The Astrophysical Journal, 967:168 (17pp), 2024 June 1 https://doi.org/10.3847/1538-4357/ad3d5a
© 2024. The Author(s). Published by the American Astronomical Society.
OPEN ACCESS

PROJECT-J: JWST Observations of HH46 IRS and Its Outflow. Overview and First Results

Brunella Nisini[1], Maria Gabriela Navarro[1], Teresa Giannini[1], Simone Antoniucci[1], Patrick, J. Kavanagh[2], Patrick Hartigan[3], Francesca Bacciotti[4], Alessio Caratti o Garatti[5], Alberto Noriega-Crespo[6], Ewine F. van Dishoeck[7], Emma T. Whelan[8], Hector G. Arce[9], Sylvie Cabrit[10,11], Deirdre Coffey[12], Davide Fedele[4], Jochen Eislöffel[13], Maria Elisabetta Palumbo[14], Linda Podio[4], Tom P. Ray[15], Megan Schultze[3], Riccardo G. Urso[14], Juan M. Alcalá[5], Manuel A. Bautista[16], Claudio Codella[4], Thomas P. Greene[17], and Carlo F. Manara[18]
[1] INAF—Osservatorio Astronomico di Roma, Via di Frascati 33, 00078 Monte Porzio Catone, Italy; brunella.nisini@inaf.it
[2] Department of Experimental Physics, Maynooth University, Maynooth, Co Kildare, Ireland
[3] Physics and Astronomy Dept., Rice University, 6100 S. Main Street, Houston, TX 77005-1892, USA
[4] INAF—Osservatorio Astrofisico di Arcetri, Largo E. Fermi 5, I-50125 Firenze, Italy
[5] INAF—Osservatorio Astronomico di Capodimonte, via Moiariello 16, 80131 Napoli, Italy
[6] Space Telescope Science Institute, 3700 San Martin Drive, Baltimore, MD 21218, USA
[7] Leiden Observatory, Leiden University, PO Box 9513, NL 2300, RA Leiden, The Netherlands
[8] Department of Experimental Physics, Maynooth University, Maynooth Co. Kildare, Ireland
[9] Department of Astronomy, Yale University, New Haven, CT 06511, USA
[10] LERMA, Observatoire de Paris-PSL, Sorbonne Université, CNRS, F-75014 Paris, France
[11] IPAG, Observatoire de Grenoble, Université Grenoble-Alpes, France
[12] University College Dublin, School of Physics, Belfield, Dublin 4, Ireland
[13] Thüringer Landessternwarte, Sternwarte 5, D-07778 Tautenburg, Germany
[14] INAF—Osservatorio Astrofisico di Catania, via Santa Sofia 78, 95123, Catania, Italy
[15] Dublin Institute for Advanced Studies, 31 Fitzwilliam Place, D02 XF86, Dublin, Ireland
[16] Department of Physics, Western Michigan University, Kalamazoo, MI 49008, USA
[17] NASA Ames Research Center, MS 245-6, Moffett Field, CA 94035, USA
[18] European Southern Observatory, Karl-Schwarzschild-Strasse 2, 85748 Garching, Germany
Received 2024 January 17; revised 2024 April 9; accepted 2024 April 9; published 2024 May 30

Abstract

We present the first results of the JWST program PROJECT-J (PROtostellar JEts Cradle Tested with JWST), designed to study the Class I source HH46 IRS and its outflow through NIRSpec and MIRI spectroscopy (1.66–28 μm). The data provide line images ($\sim$6.″6 in length with NIRSpec, and up to $\sim$20″ with MIRI) revealing unprecedented details within the jet, the molecular outflow, and the cavity. We detect, for the first time, the redshifted jet within $\sim$90 au from the source. Dozens of shock-excited forbidden lines are observed, including highly ionized species such as [Ne III] 15.5 μm, suggesting that the gas is excited by high velocity (>80 km s^{-1}) shocks in a relatively high-density medium. Images of H_2 lines at different excitations outline a complex molecular flow, where a bright cavity, molecular shells, and a jet-driven bow shock interact with and are shaped by the ambient conditions. Additional NIRCam 2 μm images resolve the HH46 IRS $\sim$110 au binary system and suggest that the large asymmetries observed between the jet and the H_2 wide-angle emission could be due to two separate outflows being driven by the two sources. The spectra of the unresolved binary show deep ice bands and plenty of gaseous lines in absorption, likely originating in a cold envelope or disk. In conclusion, JWST has unraveled for the first time the origin of the HH46 IRS complex outflow demonstrating its capability to investigate embedded regions around young stars, which remain elusive even at near-IR wavelengths.

Unified Astronomy Thesaurus concepts: Young stellar objects (1834); Protostars (1302); Stellar jets (1607); Infrared spectroscopy (2285); Protoplanetary disks (1300)

1. Introduction

The study of protostars and their planet-forming disks is inseparable from understanding the role and properties of their associated outflows. Protostellar systems include several components (i.e., the stellar object, a compact and massive accretion disk, and a dusty envelope) but the most prominent phenomenon is mass ejection in the form of powerful jets and winds. Their strong line emission extends up to parsec scales from the protostar and dominates the spectrum at almost all wavelengths (Frank et al. 2014; Bally 2016). It is now widely accepted that jets are magnetocentrifugally launched from an inner star-disk interaction region (e.g., Pelletier & Pudritz 1992), although the details of the mechanism are still poorly constrained, especially during the early phases of stellar evolution. According to MHD disk-wind models (see, e.g., Ferreira 1997; Bai et al. 2016), matter is extracted at different spatial radii from the disk surface. These ejections remove disk mass and angular momentum, and thus they have a fundamental role in driving accretion and determining the timescale of disk dispersal. The high-velocity (200–400 km s^{-1}) collimated jets are launched from the very inner regions of the disk (on scales of a few 0.1 au), however mass loss in the form of less collimated and slow flows (10–30 km s^{-1}) might involve a large portion of the disk (up to several tens of au), thus affecting the disk physics and influencing the formation of planetary systems (e.g., Pascucci et al. 2023). Alternative models, such as

Original content from this work may be used under the terms of the Creative Commons Attribution 4.0 licence. Any further distribution of this work must maintain attribution to the author(s) and the title of the work, journal citation and DOI.

the X-wind model, assume that the outflow originates from a small region at the interface between the inner edge of the disk and the stellar magnetosphere. They also predict the formation of a collimated high-velocity outflow surrounded by a wide-angle wind (Shang et al. 2020). The manner in which jets and winds are launched and propagate also influences their feedback on the ambient medium and envelope dispersal during the early stages with the typical creation of large cavities in the infalling envelopes and the entrainment of the cold ambient gas (e.g., Rabenanahary et al. 2022; Shang et al. 2023) which is observed in the submillimeter by, e.g., the Atacama Large Millimeter/submillimeter Array (ALMA; e.g., Arce et al. 2013; de Valon et al. 2022).

To get insights into these different mechanisms one needs to peer into regions within a few hundred astronomical units from the central star, where the outflows preserve the pristine information about their velocity, collimation mechanism, and connection with accretion events. However, during the critical stage of protostellar vigorous accretion, the innermost regions of the jet are still deeply embedded in their dusty envelope making their investigation at high angular resolution challenging. Additionally, when studying outflows in young stellar objects (YSOs) of different ages, one should bear in mind that the physical conditions of both the ejections and the environment through which the flow travels vary considerably during evolution. Consequently, the choice of observational tracers should be carefully tailored depending on the source. In particular, while jets in more evolved and less extincted Classical T Tauri stars (CTTs, Class II sources) have mostly been studied with optical forbidden lines, the origin of outflows from embedded Class 0 and Class I protostars (ages $1–10 \times 10^4$ yr) needs to be investigated in the IR and submillimeter domain, as this is the spectral range where most of the outflowing gas is emitting. For the youngest and deeply embedded Class 0 sources, high-resolution submillimeter observations with ALMA are getting insights into the mostly molecular and cold jets (e.g., Lee 2020; Podio et al. 2021). However, the warmest gas component expected to be excited, either by shocks or by the action of UV photons, along protostellar flows and associated cavities is best traced through IR atomic and molecular lines (Frank et al. 2014), as highlighted by observations with previous space facilities such as the Infrared Space Observatory (ISO), and the Spitzer and Herschel satellites (e.g., Nisini 2003; Giannini et al. 2011; Nisini et al. 2016; Watson et al. 2016). It is however only thanks to the superb resolution and sensitivity of the James Webb Space Telescope (JWST) that it is now possible to investigate the launching mechanism of jets/outflows in the earliest stages, and their feedback on the ambient medium, with the same level of accuracy as currently achieved only in the optical for the more evolved CTT stars.

JWST observations of Class 0 sources are indeed now giving unprecedented details on the morphology and composition of their jets, wide-angle molecular flows, and cavities (e.g., Federman et al. 2024), although in the youngest of these protostars, their highly embedded innermost region can be hardly traced even at mid-IR wavelengths (Ray et al. 2023). On the other hand, JWST is best suited for the study of the intermediate age Class I objects (age $\sim 10^5$ yr), which are still actively accreting from a massive disk, but their parental envelope, within which they are still embedded, can be easily penetrated at mid-IR wavelengths. This in fact makes the Class I sources the only sources during the young star's evolution where all the actors involved, namely the fast axial jet, the wide-angle slow wind, the accreting protostar, and the inner disk region, can be all efficiently studied with JWST.

With this in mind, we present here the PROtostellar JEts Cradle Tested with JWST (PROJECT-J) project, a Cycle 1 GO program aiming at studying the Class I protostar HH46 IRS and its outflow system through integral field spectroscopy (IFU) observations from 1.7 to 28 μm with NIRSpec and MIRI. The main aim of the project is to disentangle the proposed mechanisms at the origin of the outflow and the associated cavity. This will be achieved by providing a unified view of all the outflow components pertaining to this paradigmatic Class I system, and connecting them with the accretion and stellar properties of the central object, which can now be characterized in the mid-IR. This paper provides a general overview of the program, describes the reduction and quality of the acquired data, and highlights its main outcomes. A more detailed analysis of the different scientific topics will be presented in specific papers currently in preparation. The paper is structured as follows: Section 1.1 gives an overview of the HH46 source and its outflow; Section 2 presents the observations and data reduction for the MIRI (Section 2.1) and NIRSPEC (Section 2.2) data set, with a focus on the process adopted to produce spectra (Section 2.3) and line emission maps (Section 2.4); Section 3 illustrates the results concerning the outflow, i.e., the line maps of the atomic jet (Section 3.1), and the molecular outflow and cavity (Section 3.2); Section 4 presents the spectrum of the protostar; finally, Section 5 presents the main conclusions of the performed study.

1.1. HH46 IRS and Its Outflow

HH46 IRS (2MASSJ08254384-5100326) is a low mass Class I source, ($M \sim 1.2 M_\odot$, $L_{\rm bol} < 15\ L_\odot$, Antoniucci et al. 2008), located in a Bok globule at the edge of the Gum Nebula ($d = 450$ pc). Hubble Space Telescope (HST) observations suggest that the source is actually an embedded binary system with a projected separation of 0.″26 (~120 au; Reipurth et al. 2000). The source drives a parsec scale chain of Herbig Haro (HH) objects known as the HH46/47 outflow system, which has been studied at both optical (e.g., Eislöffel & Mundt 1994; Heathcote et al. 1996; Hartigan et al. 2011) and infrared wavelengths (e.g., Eislöffel et al. 1994; Reipurth et al. 2000; Noriega-Crespo et al. 2004; Erkal et al. 2021). The optically bright HH46/47 jet is part of the northeast flow and terminates in the HH 47A bow shock at about 1.′3 from the source. Multiepoch HST observations of this jet have shown that the jet moves at $\sim 300\ {\rm km\ s^{-1}}$ and it is inclined by about 37° with respect to the plane of the sky (Hartigan et al. 2005). The jet presents a large wiggling morphology, believed to originate from precession around a tertiary nonresolved source (Reipurth et al. 2000), which also causes a change with time of the jet orientation angle of about 15° (Hartigan et al. 2005). A fainter counter-jet in the redshifted southwestern lobe (Eislöffel et al. 1994; Velusamy et al. 2007) extends toward the bow shock HH 47C. Recent deep [Fe II] HST images of the outflow have revealed unprecedented details of the inner region of the jet, showing that the blueshifted jet is formed by several collimated emission knots displaced along an arc-shaped pattern that follows the general curved morphology at larger scales (Erkal et al. 2021). Even in the near-IR, the redshifted jet remains obscured close to the source and only emerges at a distance of about 5″ appearing highly misaligned with respect to the blueshifted jet. This redshifted jet has also been detected at

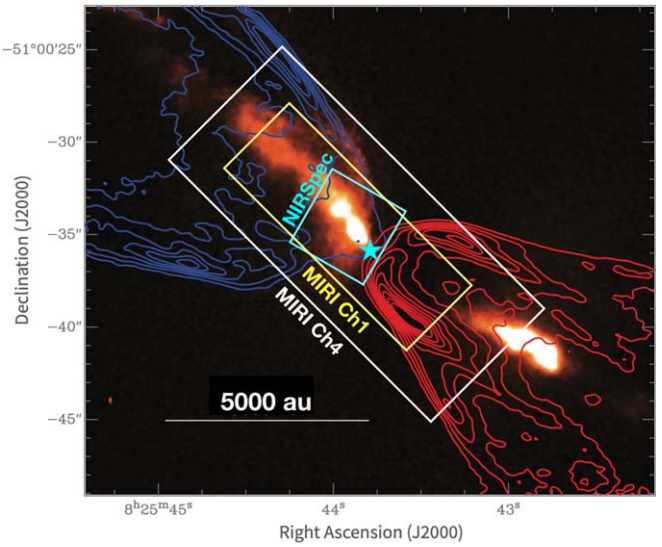

Figure 1. HST WFC3 continuum-subtracted [Fe II] 1.64 μm image (Erkal et al. 2021) of the HH46 jet, with overlaid contours of the ALMA CO 1−0 redshifted (red contours) and blueshifted (blue contours) emission from Arce et al. (2013). The cyan box indicates the region covered by the NIRSpec mosaic while for MIRI the smallest and the largest fields of view covered by Channel 1 and 4 are indicated by the yellow and white boxes, respectively.

mid- and far-IR wavelengths although at low spatial resolution (Velusamy et al. 2007; Nisini et al. 2015). The large contamination from the central source however prevents tracing the counter-jet close to the source in these images. The large-scale HH46 IRS outflow has been mapped at submillimeter wavelengths in CO 6–7 and [C I] 2-1 by van Kempen et al. (2009), who suggested that the excitation of these lines could be due to ultraviolet photons originating in the jet shocks.

Recently, the HH46 IRS outflow has been studied via high angular resolution ALMA observations of CO 1−0 (Arce et al. 2013; Zhang et al. 2016) and CO 2-1 (Zhang et al. 2019). These observations have shown the presence of nested shell-like structures of cold molecular gas displaying a regular velocity pattern, such that the higher velocity structures extend further from the source. It has been suggested that such a shell-like outflow is due to the entrainment of ambient gas by a series of outbursts from an intermittent wide-angle wind (Zhang et al. 2019), or, alternatively, by a pulsed narrow jet (Rabenanahary et al. 2022). The unified picture connecting the HH46 IRS outflow and jet, which JWST is for the first time able to provide, will clarify the different scenarios for the origin of the complex mass ejection mechanism in this source.

2. Observations and Data Reduction

We mapped the HH46 IRS source and its outflows as part of the JWST Cycle 1 program PROJECT-J (ID 1706, P.I. B. Nisini) with the instruments NIRSpec IFU (Böker et al. 2022; Jakobsen et al. 2022) and MIRI MRS (Rieke et al. 2015; Wright et al. 2023). Figure 1 shows the regions mapped with the two instruments, which include the central source, the jet and counter-jet, and the wide-angle cavity traced by ALMA observations. The data were taken on 2023 February 16 and 19 with NIRSpec and on 2023 March 3 with MIRI. Details on the adopted settings and data reduction procedures are given in Subsections 2.1–2.4.

2.1. MIRI

The MIRI MRS mode adopted for the observations uses four integral field units (IFUs) referred to as channels, to continuously cover the spectral range between 4.9 and 27.9 μm. Each channel is divided into three subbands named SHORT, MEDIUM and LONG. The spatial sampling of the four channels is 0.″196, 0.″196, 0.″245 and 0.″273 per pixel, therefore each channel has a different field of view (FoV) on the sky that varies between $3.''2 \times 3.''7$ (Channel 1) and $6.''6 \times 7.''7$ (Channel 4). Figure 1 roughly indicates the smallest ($6'' \times 15''$) and largest ($\sim 11'' \times 20''$) region covered by our 4×2 map. The PA range of the observations was constrained in order to ensure the alignment of the mosaic with the outflow, allowing at the same time some flexibility for scheduling. The final PA is 47°.5 NE. The MIRI spectral resolution varies between $\sim$1500 ($V \sim 200$ km s^{-1}, Channel 4) and 3500 ($V \sim 85$ km s^{-1}, Channel 1).

The observations were taken in FAST1 readout mode with 19 groups of three integrations each, for a total of 655 s in each exposure, adopting a four-point dither pattern optimized for extended sources. The total exposure time for the full map was 4.25 hr. Simultaneous off-source MIRI imaging was conducted in the F560W filter and used for astrometric registration. A background field located in a clean region selected from the inspection of Spitzer images was observed for overall background subtraction.

The data were reprocessed using the JWST pipeline version 1.11.1 (Bushouse et al. 2023) and corresponding Calibration Reference Data System (CRDS) context jwst_1094.pmap. This version of the pipeline corrects the decrease in count rates at the MIRI MRS longest-wavelength channels reported in 2023 May.[19]

The individual raw images were first processed for detector-level corrections providing the calwebb_detector1 products (stage1). Then, astrometric correction, flat-fielding, and flux calibrations were applied using the Calwebb_spec2 module (stage 2). The individual stage 2 images were then resampled and coadded onto a final data cube through the Calwebb_spec3 processing (stage 3). In addition, the following custom steps were applied to increase the quality of the final data cube. A background subtraction was performed to the rate files, after the calwebb_detector1 stage. For that, we created a master background using the background observation rate files for each detector. The accuracy of MIRI pointing in embedded regions is affected by the paucity of suitable guide stars in the FOV. To improve the astrometric correction, we used HST + Gaia sources identified in the MIRI simultaneous imaging field, deriving a pointing adjustment of 0.″133 in R.A. and 0.″089 in decl. This correction is still subject to uncertainties in the relative astrometry between the imager and the Medium Resolution Spectrograph (MRS), which is expected to be $<0.''1$ (Patapis et al. 2024).

A significant number of warm spurious pixels are left after the calibration step 2 process, which is not removed by the stage 3 outlier_detection step. We identify them in individual exposures at the end of stage 2 using the LaCosmic algorithm developed to remove cosmic ray hits from CCD images (van Dokkum 2001). We then built a warm pixel mask for each

[19] see https://www.stsci.edu/contents/news/jwst/2023/miri-mrs-reduced-count-rate-update.

detector, that was added to the data quality (DQ) extension of the cal files after calwebb_spec2.

In the calwebb_spec2 stage we applied the residual_fringe step that corrects for the fringes due to the Fabry–Perot interference between the reflective layers of the detectors, left from the first fringe flat correction. This correction is particularly crucial for removing the residual fringe pattern from point sources, where, due to the fact that the MIRI pupil is nonuniformly illuminated, the fringe depth and phase significantly change as a function of the portion of the point-spread function (PSF) that is sampled by the detector pixels (Argyriou et al. 2023). An additional fringe correction is also applied to the final spectrum after the spectral extraction (Kavanagh et al. in prep).

2.2. NIRSpec

We performed a NIRSpec 4×2 map covering a region of about $6'' \times 6''$ centered at $08^h25^m43^s.98$, $-51°\ 00'\ 34.57''$ with a pixel scale of $0''.1$ pixel^{-1}. The PA of the mosaic is 71.2° NE. We observed with the NIRSpec gratings/filters G235H/F170LP and G395H/290LP, with a continuous coverage wavelength range between 1.66 and 5.27 μm providing a spectral resolution $R \sim 2700$ (i.e., $\sim$110 km s^{-1}). The observations were taken with an NRSIRS2RAPID readout pattern with five groups of four integrations each, using a four-point dither pattern. This implies an exposure time of 1400 s per grating in a single observation. A leakage exposure to correct for failed shutters of the NIRSpec Micro-Shutter Array (MSA) was applied. To reach the desired SNR while avoiding exceeding the data volume in a single visit, we repeated the same observing block twice. The total exposure time in each visit was 2.9 hr.

The data were processed using the JWST pipeline version 1.11.1 with the corresponding CRDS context file jwst_1094.pmap. Since calwebb_detector1 stage was stable, we ran the pipeline from the rates files. The calwebb_spec2 and three are similar to those of MIRI. We use the default parameters, carefully inspecting the intermediate products for each step. In particular, we find that the count-rate images (i.e., rate files) produced after the first stage presented significant vertical patterns associated with correlated noise, as discussed in other works using the NIRSpec IFU (e.g., Perna et al. 2023). To correct for this vertical noise, we obtained the median of each column and subtracted them. This procedure was performed in each rate file before running the calwebb_spec2 module.

Due to the lack of guide stars in the FoV, the final pointing accuracy was $\sim 0''.2$, as estimated by comparing the position of the HH46 IRS source in the G395H grating frames at $\lambda > 4$ μm, with the corresponding position in the Channel 1 of MIRI. We therefore adjusted the NIRSpec World Coordinate System solution taking the MIRI source position as a reference. The pointing adjustment resulted in $0''.114116$ in R.A. and $0''.21312$ in decl. We evaluated that no appreciable differential rotation between the NIRSpec and MIRI is present on the basis of the comparison of the overall outflow and nebula morphology at the same wavelengths.

The stage 3 outlier_detection step leaves a significant number of warm pixels. They have a particular pattern making LaCosmic not efficient in finding them, therefore we applied a different procedure to identify and remove them. In the cal files, we estimated the mean in regions of 5×7 pixels and labeled those deviating from the mean by more than 20σ as warm pixels. Remaining outliers in the cube were removed masking the unreliable flat field DQ as DO NOT USE. We then updated the DQ extension of the cal files adding these new flagged pixels. This procedure was carried out for each cal file, allowing the construction of a master warm pixel mask, that indicates the pixels that should not be used in data reduction.

2.3. Spectra Extraction and Flux Calibration

In order to check the internal consistency of the relative flux calibration between NIRSpec and MIRI subbands, we extracted a 1D spectrum at the HH46 IRS position adopting an aperture proportional to the diffraction-limited beam size (1.22λ/D) so that the aperture increases with wavelength. The source appears as point-like in both NIRSpec and MIRI images. Thus the binary detected by Reipurth et al. (2000) with a separation of $0''.26$ remains unresolved within the PSF of these instruments. We considered an aperture of 4 times the beam size in order to retrieve any flux extending beyond the diffraction-limited beam. Any larger aperture provides differences in the extracted spectrum with less than a 1% difference.

For MIRI, fluxes in the different subbands are consistent within 3% with the exception of Channel 3 MEDIUM, which has a flux 10% higher with respect to the adjacent subbands (see Appendix A). This effect is therefore not dependent on the aperture choice but appears as a pipeline issue. We eventually matched the flux between channels by the ratio of median fluxes in the overlapping wavelengths by applying scale factors starting from the shortest wavelength. Figure 14 of Appendix A shows also the Spitzer IRS spectrum of HH46 IRS from Noriega-Crespo et al. (2004), and other literature mid-IR photometric points for the source, which allows us to evaluate the global flux calibrations. The agreement between the Spitzer and the JWST spectrum decreases with wavelength, with the flux in the Spitzer spectrum at 22 μm about 50% lower than the corresponding MIRI flux. The same trend is observed also with Spitzer, WISE, and AKARI photometry. Such a large discrepancy cannot be due to calibration issues. Similar differences have been seen with MIRI MRS in other young sources (see, e.g., Gasman et al. 2023; Grant et al. 2023; Tabone et al. 2023). A possible origin for these discrepancies can reside in the intrinsic variability of the source. A certain degree of variability is shown by the mid-IR photometry taken with different facilities, although it is at a much lower level. Alternatively, it might be that the MIRI fluxes are overestimated using our nonoptimal extraction that does not take into consideration the complex PSF of the instrument. Finally, the difference could be also due to a different extraction procedure and background subtraction in the long-slit Spitzer spectrum. This issue will be further investigated in future work.

For NIRSpec, the flux within the two gratings matches better than 5% (lower panel of Figure 14 of Appendix A). There is however about a factor of 1.4 of discrepancy in the overlapping regions between NIRSpec and MIRI (see Appendix A). We rescaled the NIRSpec spectrum to the MIRI one, on the basis that in this way we also get a good agreement with the overall flux density with the Spitzer IRAC photometry at 3.6, 4.5 and 5.8 μm (see bottom panel of 14).

Overall, after rescaling the NIRSpec spectrum, we conclude that the relative calibration between NIRSpec and MIRI and among the different spectral segments is better than $\sim$5% up to $\sim$20 μm, while it can be up to 10% at longer wavelengths. The

absolute calibration has however an uncertainty of up to 40% in the on-source extracted spectrum.

2.4. Maps of Continuum-subtracted Line Emission

One of the principal aims of PROJECT-J is to provide continuum-subtracted line images of the HH46 outflow in order to study it as close as possible to the central source. This task is particularly critical at the longer wavelengths, where the PSF of the source emission dominates over a large fraction of the observed frames. Images of the continuum-free emission in individual lines have been obtained in the following way. First, a subcube covering a small wavelength range around the line of interest is created. Then we perform a linear fit through the continuum, estimated by carefully selecting a wavelength range on each side of the line free from any other emission feature. This continuum is then subtracted, pixel by pixel, in each frame of the subcube. In such a way we obtain, for each line, a continuum-free subcube that is used on the one hand to construct total line emission maps, by integrating the emission in all the spectral elements covering the line profile, and, on the other hand, to build line velocity maps. For the latter, the central wavelength of each spectral frame has been converted to velocity by comparing it to the vacuum wavelength of the considered line, after performing the correction to the local standard of rest (LSR) velocities. The $V_{\rm LSR}$ of HH46 IRS has been taken to be equal to the cloud velocity of $+5\,{\rm km\,s^{-1}}$ following Arce et al. (2013).

The linear fit of the continuum adjacent to the lines works relatively well for NIRSpec and for Channels 1 and 2 of MIRI. Above $\sim$10 μm the procedure leaves significant residual noise close to the source that compromises the identification of the line emission morphology. This is caused on the one hand by the residual fringes present at the pixel level due to the undersampling of the complex PSF morphology, and on the other hand by the significant increase of the continuum on-source level, which implies a relatively low line-to-continuum ratio for most of the lines. In order to minimize this effect, we also tried a fit with a spline function, that better traces the continuum undulation, when present. This procedure improves the situation for some of the lines, allowing us to trace the emission a few pixels closer to the source. At the longest wavelengths, however, there is a limit where the noise on the counts in the continuum exceeds the line emission, and therefore the line flux results in being under- or oversubtracted in adjacent pixels.

3. The Outflow

As shown in Figure 1 the region covered by the JWST observations includes the base of the HH46 IRS atomic blueshifted and redshifted jet, and the wide-angle cavity delineated by the CO ALMA observations. Here we separately discuss the results for these two components, that are sampled by different tracers, namely atomic forbidden lines for the jet and molecular emission for the cavity and the associated wide-angle wind.

3.1. The Atomic Jet

The MIRI spectral line images, covering a large field of view at wavelengths that suffer only limited extinction, allow us to get an understanding of the jet structure that is much improved with respect to previous optical/IR observations. Figure 2 shows the continuum-subtracted emission maps in the two brightest detected lines, namely [Fe II] 5.3μm, and [Ne II] 12.8 μm, where the main emission peaks are indicated. The knots closest to the source (B0/R0) are detected at a distance of $\sim$0.″25.

These two lines represent transitions to the ground state of the corresponding ions, excited up to levels with similar upper-level excitation energies ($\sim$1000–2000 K). However, the ionization potential (I.P) of the two species is significantly different, i.e., 7.9 eV for [Fe II] and 21.56 eV for Ne II (see Table 1). Therefore, the detection of [Ne II] lines indicates that the jet plasma is highly ionized.

The most striking result appearing from these images is that at mid-IR wavelengths the redshifted jet is clearly detected for the first time down to $\sim$90 au from the source. The 5.3 μm redshifted emission shows a collimated jet broken in several emission peaks (R0-R2) driving an extended bow shock (R3) at a distance of about 4″. The [Ne II] image, covering a larger field of view, detects an additional shocked knot (R4) located at a distance of about 7.″3. To better highlight the comparison with previous observations, we show in Figure 3 the contours of the [Fe II] 5.3 and 26 μm emission superimposed on an HST image of [Fe II] 1.64 μm (Erkal et al. 2021). The blueshifted jet has a similar morphology in the [Fe II] 1.64 and 5.3 μm lines, showing several emission peaks (named as B0-B3 in Figure 2) plus a more diffuse extended emission at larger distances. In the redshifted jet, the distinction into a jet plus a bow-shock morphology is less evident for the 26 μm emission, due to the lower MIRI spatial resolution at these wavelengths. However, due to the larger FoV of MIRI Channel 4, the 26 μm emission covers larger distances, reconnecting to the external part of the jet detected at 1.64 μm.

M. G. Navarro et al. (2024, in preparation) estimate, from the analysis of the H_2 lines, that the visual extinction in the counter-jet is >35 mag in the inner regions and gradually diminishes to values <15 mag where the jet is again detected in the near-IR. These values are consistent with the estimated on-source A_V of roughly 45 mag by Antoniucci et al. (2008).

The jet/counter-jet structure clearly does not follow a straight trajectory, and the detection of the counter-jet allows one to identify without ambiguity a mirror-like symmetry in the pattern followed by the flow, i.e., the jet trajectory in the redshifted lobe mirrors the trajectory of the blueshifted lobe. To better highlight this pattern, we show in the right panel of Figure 3 the direction of the jet axis that connects the innermost B0/R0 knots: as the jet propagates, it progressively deviates from this direction and both the blue- and redshifted knots are displaced toward the right of it. Reipurth et al. (2000) explained the wiggling pattern of the HH46 blueshifted jet as most likely due to the orbital motion of the driving source around a companion. The mirror symmetry of the redshifted jet supports this interpretation in contrast, for example, to the precession of the jet axis (e.g., Masciadri & Raga 2002). Reipurth et al. (2000) identified a binary at a 0.″26 separation in a 2 μm HST image, but concluded that the separation was too wide to explain the HH46 wiggling observed at large distances. We also point out that the identified redshifted knots R0–R3 are not displaced at exactly the same distance as the corresponding B0-B3 knots, with the exception of B0/R0. This could indicate that the location of shocked regions does not depend only on the time of the ejection events but also on the local environment encountered along the jet path. We also point

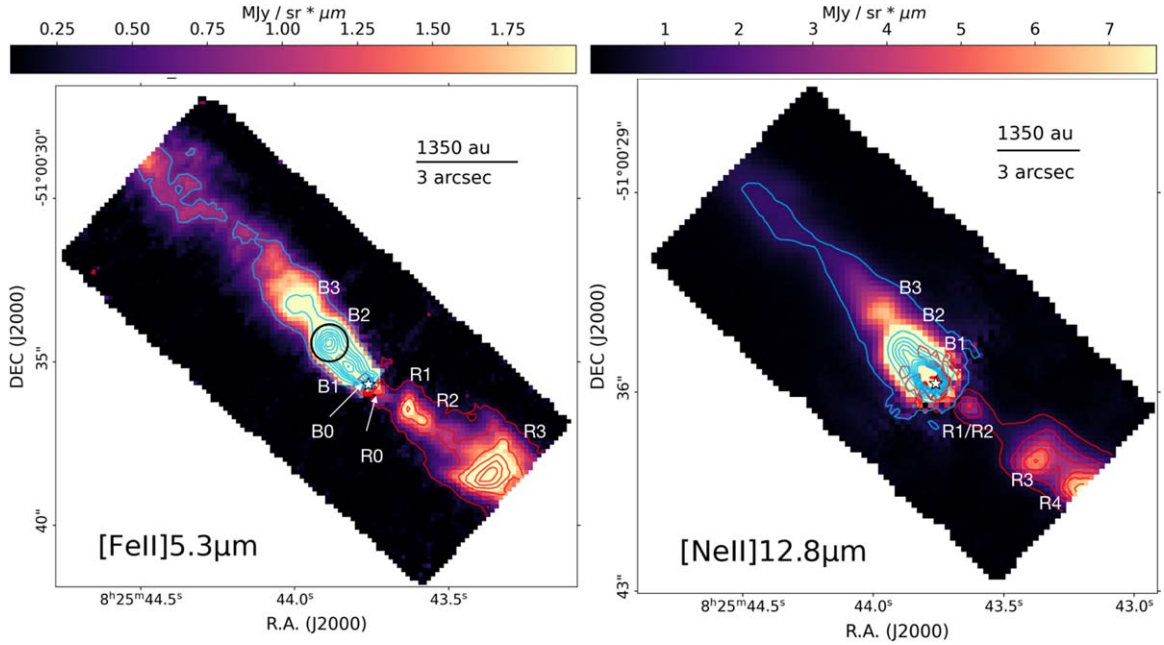

Figure 2. MIRI continuum-subtracted images of the emission in [Fe II] 5.3 μm (left) and [Ne II] 12.8 μm (right) lines. Blue and red contours delineate the blueshifted and redshifted outflow lobes, respectively. Contour levels are plotted in asinh scale and the values are as follows: [Fe II] blue from 0.8 to 12.2 MJy sr^{-1} μm, [Fe II] red from 0.3 to 4.7 MJy sr^{-1} μm, [Ne II] blue from 1.3 to 102.5 MJy sr^{-1} μm and [Ne II] red from 0.75 to 18.7 MJy sr^{-1} μm. Bright emission knots are identified in the blue- (B0-B3) and redshifted (R0–R3) jet. The black circle in the 5.3 μm image indicates the circular aperture of 0.″4 in radius from which the spectrum shown in Figure 15 has been extracted. The star indicates the position of the HH46 IRS source.

out that the NIRSpec observations do not show clear evidence for the binary detected by Reipurth et al. (2000), the separation of which is instead well sampled by the NIRCam instrumental PSF (see Section 3.2.2 and relative discussion). We devote the analysis of the jet pattern in relation to the binary motion to a future dedicated paper.

The rich atomic emission line spectrum of the HH46 IRS jet is presented in Figure 15 of Appendix B, which shows the full MIRI and NIRSpec spectrum extracted from a 0.″4 radius aperture centered on the brightest blueshifted jet knot (knot B2, see Figure 2). In addition to the many [Fe II] lines covering the entire wavelength range, we also detect the emission of several ions of other abundant elements.

Table 1 of Appendix C reports a list of the brightest detected atomic lines, including their excitation energies and the ionization potential (IP) of the corresponding ions. Noticeably, the jet appears highly ionized, as we detected bright lines of species with I.P. up to 40 eV ([Ne III]), and upper-level energy up to 3e4 K, while lines of neutral atomic species, like e.g., [S I] which dominates Spitzer spectra in other Class 0 jets (e.g., Dionatos et al. 2010), are here comparably weaker. We also detect, along the jet, several H I recombination lines of the Pa, Br, Pf, and Hu series.

The [Ne III] line emission, in particular, has a similar morphology as [Ne II] shown in Figure 2, peaking close to the source (knot B0/B1) but extending up to more than 3000au along the flow. The most likely origin for such an extended highly ionized gas is the action of high-velocity ($v > 80$ km s^{-1}) shocks, able to produce ionizing UV/X-ray photons in the postshock gas (e.g., Hartigan et al. 1987; Hollenbach & McKee 1989). Close to the source, a direct ionization from highly energetic photons from the central source could also be considered. For example, [Ne III] has been detected at the base of a few CTT jets, through its UV line at 3869 Å (e.g., Liu et al. 2016). The observation of this line in the microjet of DG Tau has been explained by photoionization due to hard X-rays produced in stellar flares, followed by slow recombination in the microjet. In HH46, the ratio [Ne II] 12.8 μm/[Ne III]15.5 μm is about 20 on knot B1, which would be consistent with both scenarios of direct UV/X-ray photoionization and shock excitation (Hollenbach & Gorti 2009). However, the [Ne III] recombination timescale is of the order of 1 yr (Glassgold et al. 2007), while the flow timescale at the distance of the B1 knot or larger is >20 yr (Hartigan et al. 2005). Therefore a different source of ionization, such as the UV/X-rays photons produced in energetic shocks, is needed to sustain the observed extended emission along the flow.

At the MIRI resolution, the kinematical structure of the jet is resolved as the jet velocity extends up to 300 km s^{-1} in either lobe (see also Garcia Lopez et al. 2010). Figure 4 presents velocity channel maps of the [Fe II] 5.3 μm and [Ne II] 12.8 μm emission. These have been obtained from our continuum-subtracted subcubes for each line, and by interpolating the frames in order to have equally spaced intervals of 30 km s^{-1}, which roughly correspond to sampling 1/3 of the MIRI spectral resolution in Channel 1.

From Figure 4 we see that close to the central source (i.e., within $\sim$3″) the jet displays a wide range of radial velocities, reaching up to 300 km s^{-1}. The jet terminal radial velocity at distances larger than $\sim$3″ is within 180–200 km s^{-1}. The observed kinematical structure is roughly consistent with the velocity measured by Garcia Lopez et al. (2010) for the [Fe II] 1.64 μm line in long-slit spectra. Considering the jet inclination of $\sim$37° with respect to the plane of the sky, the observed maximum radial velocity translates into a total jet velocity of about 380 km s^{-1}.

In spite of their different ionization potentials, the range of velocities displayed by the [Fe II] and [Ne II] lines is similar.

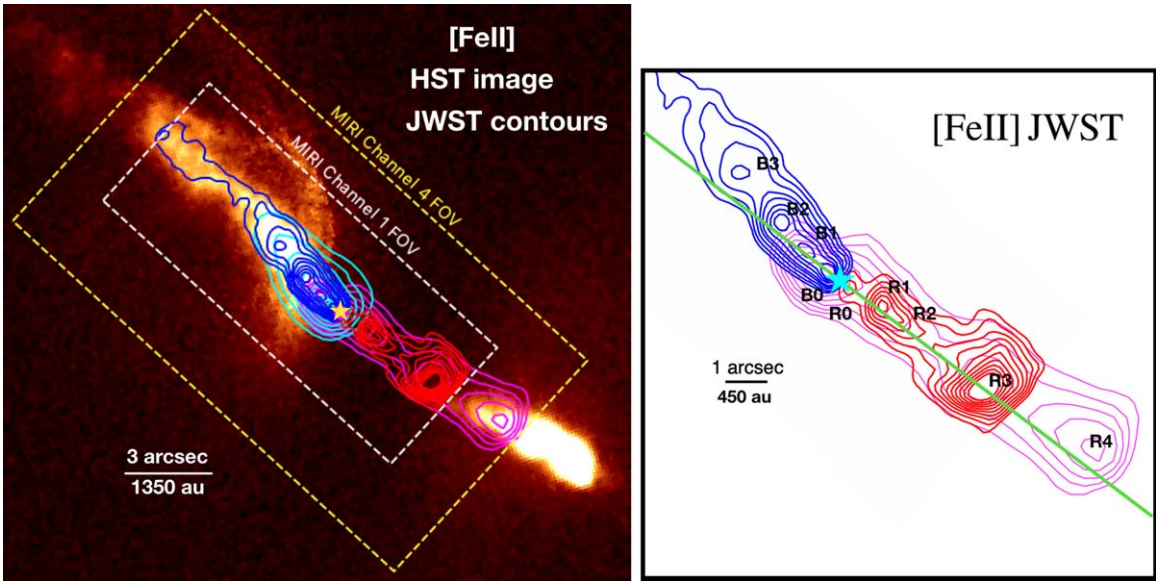

Figure 3. Left: contours of continuum-subtracted MIRI images of the [Fe II] lines at 5.3 and 26 μm are overlaid on a continuum-subtracted HST image in [Fe II] 1.64 μm from Erkal et al. (2021). The MIRI [Fe II] emissions are separately integrated into blueshifted (blue 5.3 μm, cyan 26 μm) and redshifted (red 5.3 μm, magenta 26 μm) components. The area mapped in Channel 1 and Channel 4 is highlighted. Right: contours of the inner jet region in the [Fe II]5.3 and 26 μm lines (color code as in the left panel). The main emission peaks are indicated. The green line delineates the direction of the jet axis connecting the central source with the innermost B0 and R0 knots, highlighting that the outer knots deviate from this axis with a mirror symmetry between the blue- and redshifted lobes.

However, as can also be seen in Figure 2, [Fe II] increases in brightness at a larger distance from the source, while the [Ne II] line gets fainter, indicating that the jet ionization decreases with distance. An interesting feature inferred from the [Fe II] channel maps of Figure 4 is an apparent widening of the jet with decreasing velocity.

To quantify this trend, we measured the jet width at about 1″ from the source as the FWHM of a Gaussian fit in the transversal direction, corrected for instrumental broadening ($\sqrt{\mathrm{FWHM}^2_{\mathrm{fit}} - \mathrm{FWHM}^2_{\mathrm{inst}}}$). This width linearly decreases from ∼0.″7 (315 au) in the $-90\,\mathrm{km\,s^{-1}}$ channel to 0.″39 (175 au) in the $-300\,\mathrm{km\,s^{-1}}$ channel. This is in line with the trend found in atomic jets from CTT stars observed in the optical (e.g., Maurri et al. 2014) and in molecular jets from Class 0 sources observed at millimeter wavelengths (e.g., Podio et al. 2021). The width of the jet is larger than inferred for Class II jets but similar to the width of Class 0 jets (100–500 au at low velocity and 50–250 au at high velocity at 450 au distance). The observed maximum width is in line with that measured by Erkal et al. (2021) for the HST velocity integrated [Fe II] 1.64 μm image. A detailed study of the excitation and physical properties of the jet, as a function of velocity, will be the subject of a specific paper in preparation.

3.2. The Molecular Cavity and Outflow

3.2.1. The Small Scale NIRSpec View

Figure 5 shows the NIRSpec image of the continuum-subtracted H_2 2.12 μm emission with contours of the 2 μm continuum emission (left panel) and of the [Fe II] 1.81 μm emission (right panel) overlaid. The images clearly show that the atomic and molecular emission present very different spatial distributions. In particular, we identify three main components for the H_2 extended emission delineating the edges of a parabolic cavity, two emission peaks, that we name A1 and A2, displaced at both sides of the atomic jet, and an arc-shaped structure (A3) located at the tip of the jet. Residual H_2 emission is observed also on source, as well as diffuse emission inside the cavity. The comparison with the 2 μm continuum, which shows extended emission scattered in the reflection nebula, indicates that the H_2 emission cone lies inside the cavity, at least for the north side. Part of the H_2 emission along the cavity could be due to scattered line emission originating close to the source (see, e.g., Birney et al. 2024). In addition to scattering, the H_2 emission along the cavity might originate from shocks caused by the impact of a wide-angle flow on the cavity wall or from photoevaporation (e.g., Agra-Amboage et al. 2014).

The location of the two H_2 peaks A1 and A2 might suggest at first sight that they are part of a wide-angle molecular wind around the atomic jet, brighter at the edges due to limb brightening. However, knot A2 is not oriented in the direction of the source and could be instead due to gas laterally compressed and entrained by the jet. The location of the A3 feature at the apex of the jet, and its arc-shaped morphology suggest that it could consist of material entrained as the jet is expanding. The shell morphology of knot A1, on the other hand, resembles that of an expanding bubble ejected directly from the source. The misalignment of this shell with respect to the jet axis is however puzzling and difficult to explain by environmental effects only, leaving room to the hypothesis that this structure is driven by the secondary component of the binary system (Reipurth et al. 2000), that we do not resolve with NIRSpec.

3.2.2. The Binary at the Origin of the Two Outflows?

To investigate this possibility, we used two images taken with NIRCam in the F187N and F200W filters (DDT program 4441), at a spatial resolution of 31 mas pixel^{-1}. In Figure 6 we compare the NIRSpec spectral images at 1.87 and 2.12 μm with a section of the NIRCam images covering the same region. Noticeably the NIRCam images show a weaker emission peak at a distance of 0.″23 from the main source, and roughly along the same direction where Reipurth et al. (2000) reported the

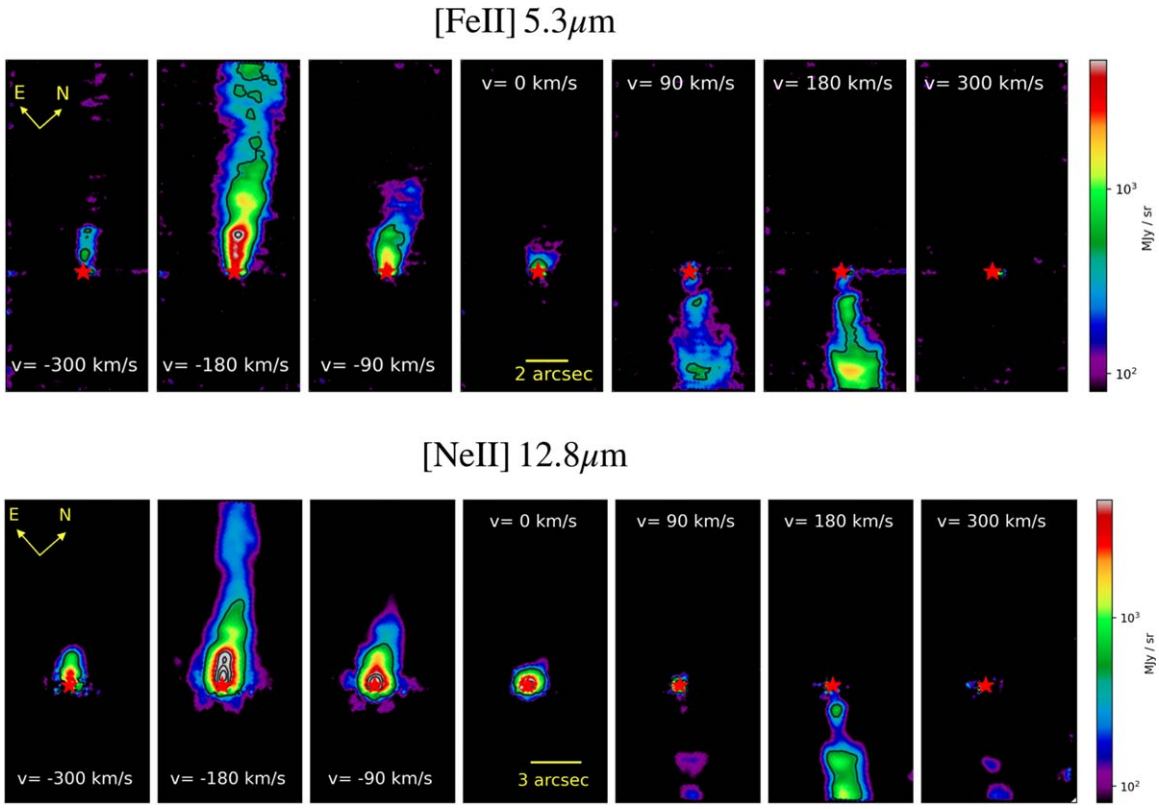

Figure 4. Velocity channel maps (integrated in 30 km s^{-1} bins) of the [Fe II] 5.3 μm (top panel) and [Ne II] 12.8 μm lines (bottom panel). The position of the central source is marked with a red star and all velocities are with respect to the systemic velocity. The images are rotated by $-48.^{\circ}5$ NW direction. Contour levels are drawn from 400 to 5×10^4 MJy sr^{-1}.

position of the companion. The lower panel of Figure 6 directly shows the comparison between the NIRCam and HST images, the latter taken about 25 yr earlier, in a similar filter. Noticeably the secondary companion, called source B by Reipurth et al. (2000), has changed its PA with respect to the primary A by about 13° counterclockwise, implying a binary period of the order of several hundred years.

The NIRCam F187N narrow filter clearly detects the jet driven by the primary source A. It also shows that the emission from the reflection nebula is divided into two parts by a dark lane, maybe a region at a higher extinction, that also obscures the initial part of the jet. The NIRCam F200W filter covers several H_2 lines and also a few [Fe II] lines. Due to the wide band and the presence of the strong nebulosity, the H_2 knots and the jet are only barely visible. In spite of that, knot A1 is well resolved and shows several substructures not resolved by NIRSpec, probably internal knots as sometimes are observed in more extended bow shocks from YSO outflows. The image clearly shows that the jet emerges from source A with a PA of ∼43° while the orientation of the A1 arc-shaped emission (PA ∼ 65°), suggests that it could instead be driven by source B. A rather similar situation has also been observed in the Class I binary TMC-1 by Tychoniec et al. (2024). An analysis of the proper motion of the A1 structure, enabled by future JWST observations, will be needed to confirm this hypothesis.

3.2.3. The Large-scale MIRI View

The MIRI observations allow us to study the distribution of the H_2 emission at larger scales, and to infer if molecular gas at low excitation, traced by the H_2 pure rotational lines covered by MIRI, displays a different morphology with respect to the warmer gas probed by the near-IR lines. Figure 7 shows the continuum-subtracted maps of the H_2 0–0 S(7) line at 5.51 μm and 0–0 S(2) line at 12.28 μm (hereafter 5.5 and 12.3 μm). The morphology of the S(7) 5.5 μm emission is very similar to that of the 2.12 μm line for the region in common, and the features A1, A2, and A3 are here also well identified. In addition, on larger scales other arc-shaped features can be seen in the blue lobe delineating the edges of additional emission shells. The map of the S(2) line at 12.3 μm better shows three blueshifted shells asymmetrically displaced with respect to the axis of the cavity, named A4, A5, and A6, together with bright diffuse emission that completely fills the cavity. In the redshifted part of the outflow H_2 emission is observed along the cavity but at a lower SNR, mainly due to extinction. The red-lobe emission is more symmetric than the blue one, and here a very bright bow shock, only barely covered by the S(7) map, largely dominates over the emission of the cavity in the S(2) emission.

In spite of the low MIRI spectral resolution, some kinematical information can be retrieved for the observed components. Figure 8 shows the spectrum of the S(7) line extracted at different positions of the blue- and redshifted lobes. Absolute wavelength calibrations do not allow us to give the radial velocity with an accuracy better than ± 30 km s^{-1}. The relative velocity shifts observed between different positions are however more reliable given the high SNR of the spectra. The blueshifted emission at both the A1 peak and the A6 arc is consistent with a velocity -30 km s^{-1}. The redshifted cavity appears shifted by about $+15$ km s^{-1} with respect to the blue outflow. In addition, we notice that the redshifted bow shock has a rather high radial velocity, reaching up to $\sim +60$ km s^{-1}.

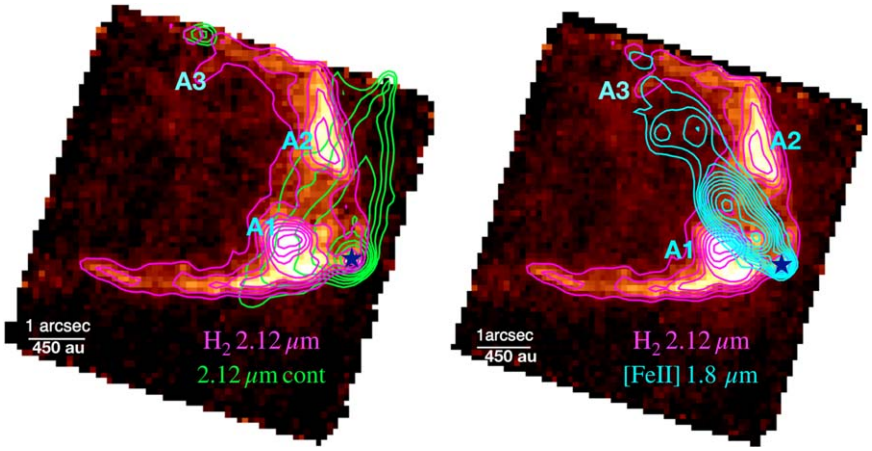

Figure 5. Continuum-subtracted NIRSpec image of the integrated H_2 2.12 μm emission of the blueshifted inner region of the HH46 IRS outflow. Overlaid contour levels go from 0.025 to 0.3 MJy sr^{-1} μm in an asinh scale. Contours of the 2.12 μm continuum emission (levels from 10 to 100 MJy sr^{-1}) are overlaid on the image in the left panel, while contours of the [Fe II] 1.8 μm emission (levels from 0.025 to 0.3 MJy sr^{-1} μm), tracing the collimated jet, are overplotted on the right panel. The H_2 knots A1–A2 and the arc-shaped feature A3 located at the apex of the jet are labeled. The blue star indicates the position of the HH46 IRS source.

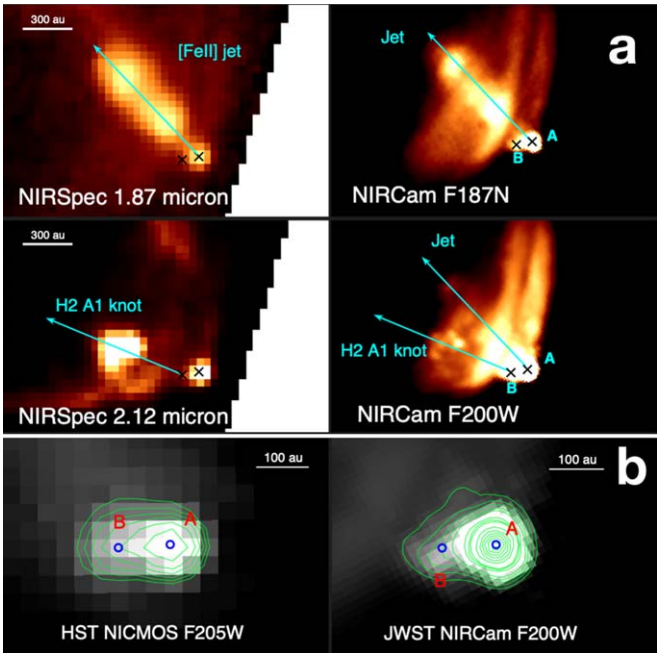

Figure 6. (a) NIRSpec images of line+continuum emission at 1.87 and 2.12 μm (left) are compared with archival NIRCam images in the F187N and F200W filters (right). The NIRCam images (spatial resolution 31 mas pixel^{-1}) reveal a secondary source (B) located at about 0.″23 from the primary (A), i.e., about the position where Reipurth et al. (2000) reported the detection of a companion. The arrows indicate the direction of the jet axis driven by source A, and the H_2 A1 arc-shaped knot apparently pointing toward source B. (b) Comparison of a HST image in the F205W filter of the HH46 IRS binary taken in 1998 with the NIRCam F200W image taken in 2023. Blue circles in both images indicate the position of sources A and B in the HST image. Source B appears to have rotated around source A by about 13° counterclockwise.

Figure 9 combines the H_2 S(2) emission with contours of the H_2 2.12 μm and [Fe II] 5.3 μm emission, for a global view of all the outflow components in the system. The morphology of the H_2 at 2.12 μm and 12.3 μm lines coincides along the cavity at the given resolution, thus we do not resolve any excitation stratification within the cavity. On the other hand, knot A1, which is bright in both the 2.12 and 5.5 μm lines, does not appear as prominent in the 12.3 μm image (as better highlighted in Figure 7). For example, on knot A1 a 2.12 μm/12.3 μm intensity ratio equal to 3.7 is observed, while the same ratio is a factor of 2 lower on knots A2 and A3. This indicates that knot A1 has a higher excitation with respect to the rest of the H_2, as also confirmed by the analysis of M. G. Navarro et al. (2024, in preparation), which find on knot A1 an H_2 temperature up to >2000 K, in contrast to other H_2 emission knots in the region where the maximum temperature is typically in the range 1500–1900 K.

Figure 16 of Appendix B shows the full MIRI and NIRSpec spectrum extracted from a 0.″4 radius aperture centered at the A1 knot (indicated in Figures 2 and 7), while Table 2 of Appendix CC summarizes the H_2 transitions detected. It can be seen that the spectrum is dominated by H_2 lines up to the $v = 3$–2 rovibrational level, covering excitation energies from ∼400 K up to ∼15,000 K. A detailed analysis of the excitation conditions in the cavity and outflow will be presented in M. G. Navarro et al. (2024, in preparation).

The comparison between the atomic jet and the molecular emission in Figure 9 shows that the cavities and outflows in the blue- and redshifted lobes appear very different. In the blueshifted cavity, the H_2 emission arcs A4/A5 and A6 do not seem to be correlated to bow shocks pushed by the jet, as they are not oriented in the jet direction (i.e., A6 arc), or apparently not associated with any jet knot. We point out that the jet is known to vary its orientation angle over time (Hartigan et al. 2005) due to its wiggling; however, the opening angle of the precession is about ± 15° around the jet axis, thus much lower than, e.g., the angular distance between the jet axis and the A6 arc, which is around 25°. In addition, the cooling time of the H_2 12.3 μm line is of the order of 70 yr, in contrast with the more than 200 yr ages of the jet knots located at further distances with proper motion deflected toward SE with respect to the present direction (e.g., knots Jh5/Js7, Hartigan et al. 2005).

It is therefore unlikely that the H_2 shells, as well as the misalignment of the jet with respect to the cavity, originate from the jet precession only. On the other hand, the A6 arc is roughly oriented in the direction of the A1 knot, (i.e., the IRS-B source, A1, and the apex of the A6 arc are aligned with an angle of ∼64°) and shares with it the same radial velocity, giving support to the possibility that the large-scale H_2 arcs, (or at least the A6 arc), originate, as the A1 knot, from expanding

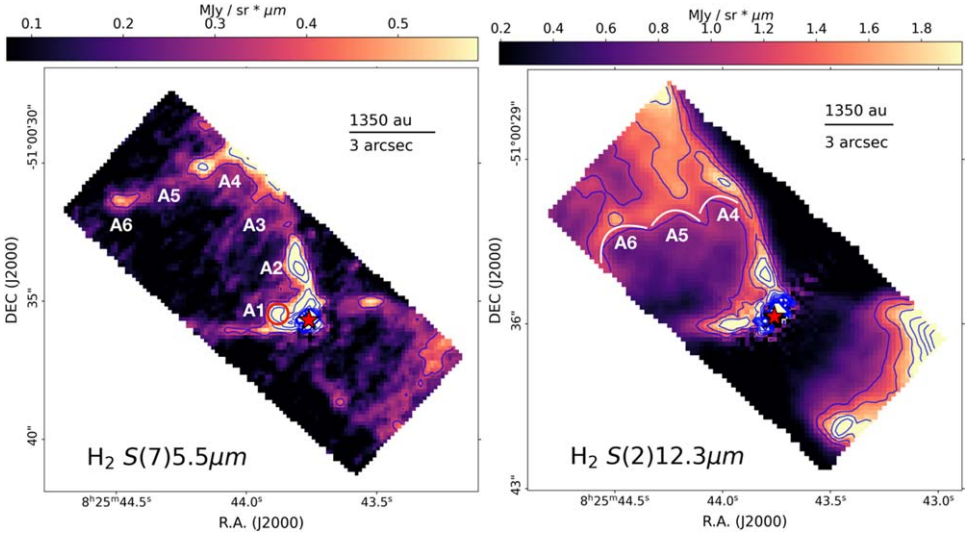

Figure 7. MIRI continuum-subtracted images of the emission in the H_2 0–0 S(7) line at 5.5 μm (left) and 0–0 S(2) line at 12.3 μm (right). A Gaussian smoothing with $\sigma = 0.5$ has been applied to both images. Contour levels are drawn in an asinh scale as follows: 5.5 μm from 0.36 to 2.42 MJy sr^{-1} μm, 12.3 μm from 1.07 to 6.65 MJy sr^{-1} μm. The main H_2 knots (A1–A2) and arc-shaped features (A3-A6) are indicated. The red circle indicates the aperture (0.″4 in radius) from which the spectrum shown in Figure 16 has been extracted.

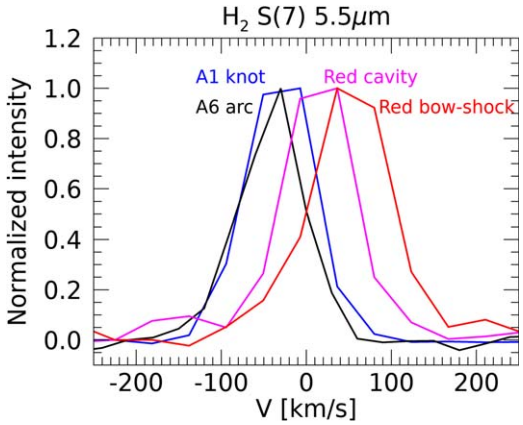

Figure 8. Spectra of the H_2 5.5 μm line extracted in selected positions of the blueshifted and redshifted outflow.

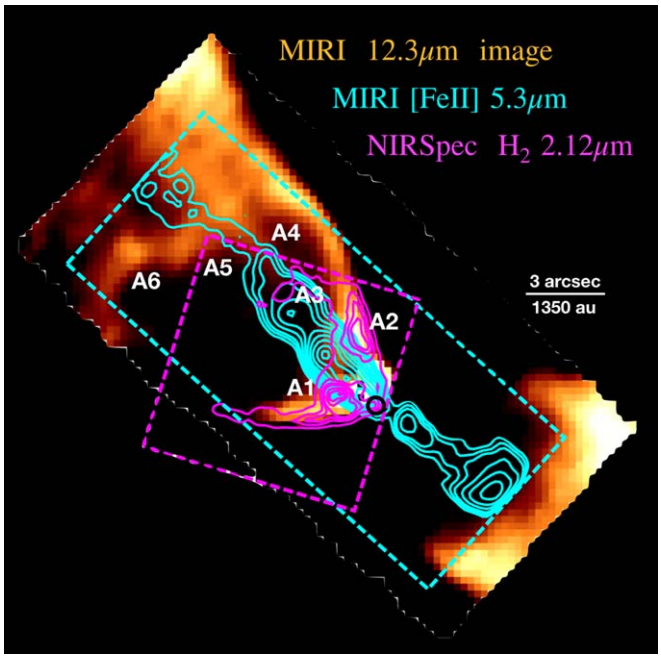

Figure 9. Continuum-subtracted image of the H_2 0–0 S(2) 12.3 μm line with overlaid contours of the H_2 1–0 S(1) 2.12 μm observed by NIRSpec (magenta) and [Fe II] 5.3 μm emission from the jet (cyan). Labels indicate the A1–A6 H_2 knots and arcs discussed in the text. The figure shows the similar morphology displayed by the rotational and rovibrational lines. It also suggests that the extended H_2 emission in the redshifted outflow corresponds to a large bow shock driven by the atomic jet. In contrast, the arc-shaped structures A5–A6 on the blueshifted side are not oriented along the jet axis.

shells ejected by the source B of the binary system. Precession and environmental effects might additionally contribute to shaping the overall morphology of the blueshifted cavity as it appears in the H_2 images. Noticeably there are no similar structures within the redshifted cavity. Here, the large molecular bow shock delineated by the H_2 S(2) 12.3 μm emission is clearly correlated with the smaller size atomic bow shock seen in [Fe II] 5.3 μm. This latter shock may represent a Mach disk where the supersonic jet is decelerated and heated in a fast shock, which drives a slower nondissociative bow shock, seen in H_2, into the ambient molecular material.

3.2.4. Comparison between H_2 and CO ALMA Observations

The large asymmetries in structure and shape between the blue- and redshifted cavities observed in H_2 emission, were also highlighted in the CO outflow observed with ALMA. Arce et al. (2013) pointed out that the different morphology and opening angles of the blue- and redshifted CO cavities could be due to different ambient densities encountered by the outflows in the two lobes. Given the location of HH46 at the edge of a globule, the blueshifted flow travels more freely in a lower-density environment, while the redshifted outflow encounters a high-density region and thus entrains a larger amount of material.

To better compare the morphology of the warm molecular emission with that of the cold CO gas, we overlay in Figure 10 the ALMA ^{12}CO 2-1 at velocity $\pm$ 9 km s^{-1} (cloud corrected) with the H_2 S(7) 5.5 μm and S(1) 17 μm images. This latter image covers the largest area mapped with MIRI. As shown in Zhang et al. (2019), the ^{12}CO 2-1 outflow presents several

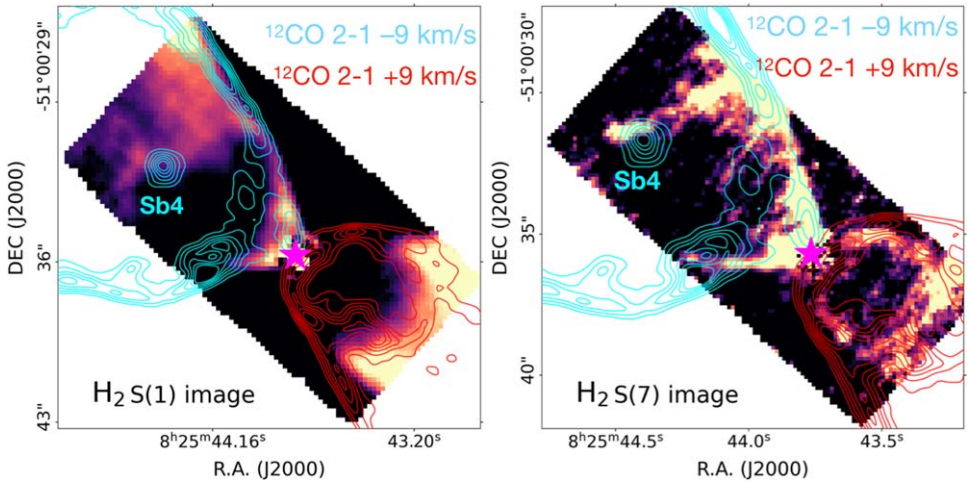

Figure 10. MIRI images of the emission in the H_2 0–0 S(1) and S(7) lines with contours of the ALMA ^{12}CO 2-1 emission in the velocity channels at $V_{LSR} \pm 9$ km s^{-1} (integrated within 1 km s^{-1}). CO contour levels are drawn in linear scales and have the following values: redshifted from 0.05 to 0.24 K km s^{-1}, and blueshifted from 0.02 to 0.11 K km s^{-1}. The resolution of the ALMA observations is $0\farcs67 \times 0\farcs48$.

emission shells traveling at different velocities, with the higher outflow velocities extending farther from the source with respect to the lower velocities. We make here the comparison with a single CO low-velocity channel as this roughly corresponds to the first observed structured shell, covering the region mapped with MIRI, and traces the cavity walls (Figure 3 of Zhang et al. 2019), for a direct comparison between the H_2 and CO cavities. We see that the H_2 emission observed along the cavity is inside the CO emission in both lobes. This is particularly evident in the redshifted cavity when comparing the H_2 S(7) and the CO morphology. This warm emission associated with the cavity could be driven by shocks or by photon heating of the cavity walls. Heating of the outflow cavity walls by ultraviolet photons originating from the jet shocks and accretion disk was also proposed to explain the far-IR and submillimeter observations of high-J lines of CO, H_2O, and OH along the outflow (van Kempen et al. 2009, 2010).

The H_2 and CO emissions are instead spatially overlapping only in the northern part of the blueshifted cavity. This could be due to the fact that in this direction the flow encounters a larger density and thus the gas cannot expand freely. The H_2 shells in the blue cavity are not clearly associated with any CO emission shells, although a CO peak, called Sb4 in Zhang et al. (2019), is roughly coincident with the A6 arc. In the redshifted lobe, the large H_2 bow shock is located further away with respect to the CO shell at 9 km s^{-1}. However, as previously pointed out, the CO emission presents shells at a larger distance from the source as the velocity increases. Therefore the CO at 9 km s^{-1} is probably not kinematically linked with the H_2 bow shock, as this latter is traveling at much higher velocity.

Zhang et al. (2019) interpreted the CO shells morphology and velocity distribution as due to material swept up by an outbursting wide-angle wind. In this framework, the different shells could originate from each intermittent mass ejection episode. Zhang et al. (2016) in addition suggest that the redshifted outflow can also be consistent with a bow-shock entrainment, where the jet might expand and laterally push ambient material creating a wide cavity with low collimation. Indeed, models of pulsed jet-driven shells are qualitatively able to reproduce the morphological and kinematical features of the HH46 redshifted cavity (Rabenanahary et al. 2022). The MIRI observations reinforce this interpretation as we observe for the first time the inner jet and the bow shock, symmetrically located inside the cavity.

As discussed before, for the blueshifted outflow it is unlikely that jet-driven bow shocks are the only driving mechanism at the origin of the CO entrainment and the complex system of H_2 shells seen with MIRI, although the spatial correspondence of a jet knot with the A3 shell seen in Figure 5 suggests that the jet contributes to push material sideways in the NE direction. The evidence, however, that further out the outflow is not apparently associated with any jet knots, supports the hypothesis that the large cavity and associated H_2 emission originate from a wide-angle molecular wind, that we suggest is launched by source B of the binary, although precession and interaction with the surrounding material might also play a role in shaping the overall cavity.

4. The Spectrum of the HH46 IRS Protostar

Figure 11 shows the complete NIRSpec + MIRI spectrum extracted at the source position as described in Section 2.3. The spectrum steeply rises with wavelength and shows several absorption features due to ices and dust species. We clearly detect the 9.7 μm silicate band, as well as strong features of abundant molecules, such as H_2O, CO_2, CH_3OH, NH_3, OCN^-, some of them already observed in the Spitzer intensified Reticon spectrograph (IRS) spectrum of the source (Boogert et al. 2004; Noriega-Crespo et al. 2004). In addition, thanks to the higher sensitivity and spectral resolution provided by JWST, we are able to detect weaker features due to less abundant and more complex organic molecules (COMs). As an example, the bottom inset of Figure 11 shows the range 5.5–8 μm where, in addition to the broad 6 μm band attributed to the bending mode of H_2O, we also note a peak at 5.83 μm that might arise from the presence of molecules bearing a C = O bond, such as HCOOH/H_2CO (e.g., Yang et al. 2022; Rocha et al. 2024). Also, the 6.78 μm band can be attributed to various compounds, including NH_3, NH_4^+, and other species bearing carboxyl and CH groups. This feature also shows additional peaks at 7.256 and 7.376 μm that are attributed to $HCOO^-$, with possible contributions from more complex compounds, such as amides and aldehydes (Urso et al. 2022),

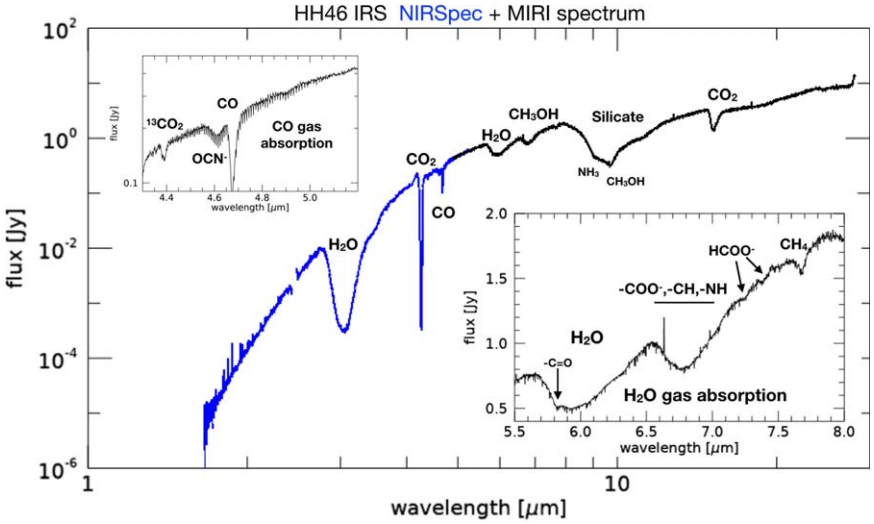

Figure 11. NIRSpec and MIRI MRS spectrum extracted at the position of HH46 IRS point source, with major solid-state features indicated. Insets show details of the 4.5 and 6.5 μm regions from the same spectrum where numerous rotational transitions of CO and H_2O are detected in absorption.

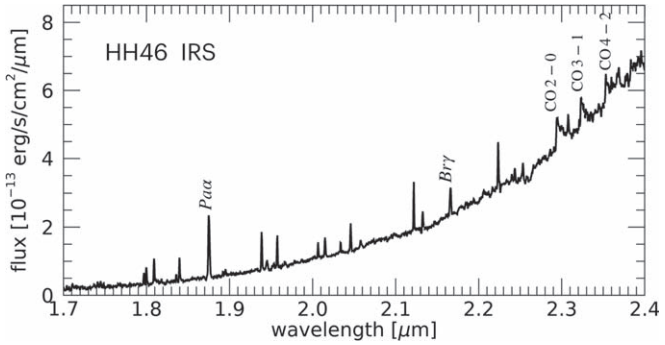

Figure 12. Section of the HH46 IRS NIRSpec spectrum around 2 μm. H I lines and CO overtone emission lines are indicated.

that have been observed in other protostars (e.g., Yang et al. 2022; McClure et al. 2023; Rocha et al. 2024).

A peculiarity of this spectrum is the detection of many gas features seen in absorption instead of emission, at variance with the JWST spectra of other low-mass protostars (e.g., Yang et al. 2022; Federman et al. 2024). This can be seen for example in the upper inset of Figure 11, which highlights the spectral region around 4.5 μm, where absorption lines from the CO rovibrational transitions of the $v = 1-0$ fundamental band are detected, and in the bottom inset covering the range 5.5–8 μm where many additional absorption lines, mostly from H_2O are present (e.g., Gasman et al. 2023). We remark that the CO $v = 1-0$ lines are instead detected mostly in emission in the outflow, as can be seen in Figures 15 and 16 of Appendix B. This indicates that the line absorption could arise in the dense molecular envelope surrounding the young stellar object, as found in a number of high-mass protostars by observations with the Infrared Space Observatory (e.g., Helmich et al. 1996), and recently also with JWST (Francis et al. 2024). Alternatively, given the relatively high inclination of the putative disk (i.e., 53°, if perpendicular to the jet orientation), the observed lines could also originate on the surface layer of an outer flared disk, that intercepts the mid-IR photons of the warm inner disk region. Strong absorption in the CO $v = 1-0$ lines has indeed also been observed in some T Tauri stars and apparently correlates with the disk inclination (Banzatti et al. 2022). A detailed analysis of the gas excitation conditions is required to disentangle these possibilities, which is deferred to a dedicated paper.

Figure 12 shows a zoom of the NIRSpec spectrum around the 2 μm range. This can be compared with the spectrum obtained from the ground using 8 m telescopes (Antoniucci et al. 2008; Birney et al. 2024). Even with the larger SNR attained with NIRSpec with respect to the ground-based observations, no photospheric absorption lines (e.g., Nisini et al. 2005; Greene et al. 2018) are detected here, which implies that the IR line and continuum emission from the disk and accretion spots dominate and completely veil the stellar photosphere. The CO overtone bandheads ($\Delta v = 2$) are detected in emission, at variance with the lines of the fundamental vibrational band detected in absorption. These overtone emission lines are rarely detected from T Tauri disks, but are often displayed by highly accreting Class I sources. The detection of the CO bandheads implies a kinetic temperature of a few thousand Kelvin and their emission likely originates from the hot gas in the innermost disk region.

In the HH46 IRS spectrum, we detected four H I lines, namely Paα at 1.88 μm, Brγ at 2.16 μm, Brβ at 2.62 μm, and Brα at 4.05 μm. Pfund and Humphrey lines covered in the MIRI range and seen in the outflow (see Table 1) are not detected on source at more than the 2σ level due to the low line/continuum ratio. Figure 13 shows the profiles of the detected lines ordered by increasing energy of the upper level. It can be noticed that the peak of the line shifts from about $-150\,\mathrm{km\,s^{-1}}$ for the less energetic lines (Paα and Brα), to about $0\,\mathrm{km\,s^{-1}}$ for the lines at higher energy (Brγ and Brβ). This shows that the line emission shifts from being outflow dominated to being accretion dominated, depending on the excitation condition. The ionized jet at its base significantly contributes to the H I emission of the low-level lines of each series, while higher-level lines of the same series are dominated by emission from the higher density gas of the accretion columns, which causes an increase of the line optical depth and thus a deviation from the optically thin Case B (Antoniucci et al. 2017). We point out, however, that the jet still contributes, even if at a lower level, to the emission of high excited lines

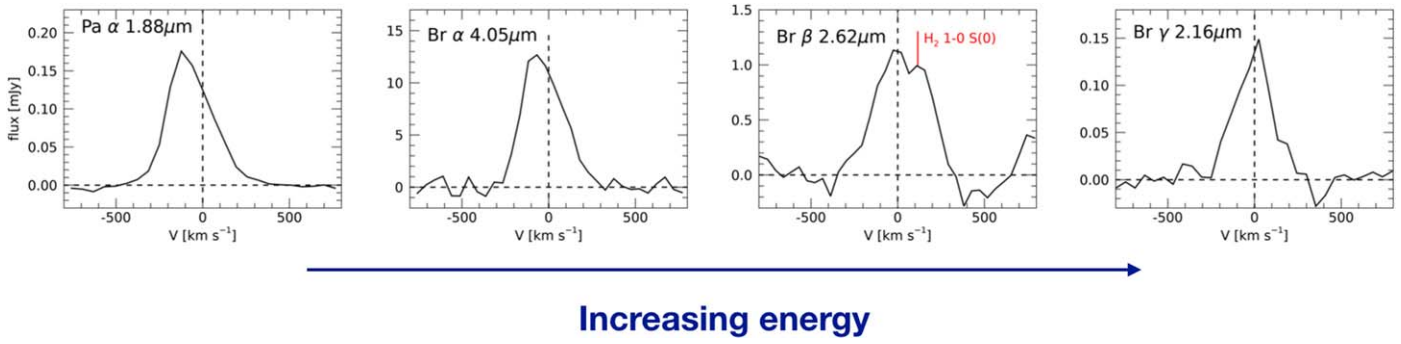

Figure 13. Hydrogen recombination lines detected in the HH46 IRS spectrum. The lines are ordered, from left to right, in increasing energy of the upper level. The emission peak shifts from being outflow dominated, at radial velocity ~ -150 km s^{-1}, in the lines at lower energy, to being accretion dominated ($V \sim 0$ km s^{-1}) in the higher energy transitions.

such as the Brγ line, as this emission at high velocity is spatially extended, as also shown in Birney et al. (2024).

In low-mass T Tauri stars, optical and IR hydrogen recombination lines are commonly used to derive the source accretion luminosity ($L_{\rm acc}$), adopting empirical relationships that correlate the H I line luminosity with $L_{\rm acc}$ (e.g., Alcalá et al. 2017). Similar relationships have been tentatively found for lines in the mid-IR (e.g., Salyk et al. 2013; Rigliaco et al. 2015) which in principle would allow one to estimate $L_{\rm acc}$ also for very embedded young stellar objects like the Class I sources. The results we find on HH46 show that some care needs to be applied when using different lines as an independent proxy of the accretion luminosity in young sources with energetic jets, as the relative contribution of accretion and jet emission significantly changes from line to line. A detailed analysis of the accretion properties of HH46 IRS will be addressed in a future paper.

5. Conclusions

This paper presents an overview of the results obtained with JWST MIRI MRS and NIRSpec IFU observations of the Class I protostar HH46 IRS and its outflow, as part of the PROJECT-J Cycle 1 program 1706. We mapped a region of $\sim$6.″6 in length with NIRSpec, and up to $\sim$20″ with MIRI, which includes the central protostar, its collimated jet, and the associated molecular outflow and cavity. These IFU observations provide spectral maps covering the entire wavelength range from 1.66 to 28 μm at a spatial sampling between 0.″1 and 0.″3, and with a spectral resolution between 1500 and 3500. The highlights shown by these observations can be summarized as follows:

1. We detect for the first time both lobes of the atomic collimated jet to within $\sim$90 au from the source, inferring a visual extinction larger than 35 mag at the base of the redshifted counter-jet. The jet displays plenty of forbidden lines of abundant ions, the brightest two being [Fe II] at 5.3 μm and [Ne II] at 12.8 μm.

   The jet is highly ionized, as testified by the detection of several H I lines and transitions of ions such as the [Ne III] 15.5 μm and [Ar III] 8.99 μm. Such evidence indicates excitation by high-velocity (>80 km s^{-1}) shocks, although for the emission closest to the source direct ionization from UV/X-ray stellar photons cannot be excluded. No collimated molecular emission is detected along the jet.
2. We resolve the velocity structure of the jet, which shows radial velocities up to $\pm$300 km s^{-1}. Considering an inclination angle of 37°, these translate into a total jet terminal velocity of $\sim$380 km s^{-1}. Similar terminal velocities are observed in lines at different excitations. We also observe a decrease in the jet opening angle with increasing velocity. The jet width at about 1″ from the source linearly decreases from $\sim$315 au in the -90 km s^{-1} channel to 175 au in the -300 km s^{-1} channel.
3. The trajectory of the jet and counter-jet display a mirror symmetry, indicative of the orbital motion of the jet-driving source in a binary system. The morphology of the two lobes is however highly asymmetric, probably due to the different ambient medium in which the jet and counter-jet are traveling.
4. Archival NIRCam images of the central region resolve the 0.″23 binary system reported in previous HST NIR observations. The projected motion of the binary is seen here for the first time by comparing the NIRCam and HST images, acquired in a time span difference of 25 yr, and suggest a binary period of the order of several hundreds of years.
5. Spectral images of H_2 lines at different excitations outline a complex molecular flow, where the blueshifted lobe shows bright emission along the cavity, H_2 peaks uncorrelated with the collimated jet, and several large-scale molecular arcs. The NIRCam observations support the hypothesis that the observed blueshifted H_2 emission, with a morphology of an expanding shell, is driven by the companion. This evidence, together with jet precession and density gradients within the cavity could explain the large asymmetries observed between the jet, driven by the primary source, and the wide-angle molecular structures observed at a larger distance. The redshifted lobe displays weaker H_2 emission associated with a cavity and a bright jet-driven bow shock. The large asymmetry between the outflows in the two lobes is primarily due to the difference in the ambient conditions encountered by the outflow as it travels away from the source.
6. The comparison between the MIRI images and a CO ALMA low-velocity map shows emission from warm H_2 gas that follows the CO cavity but that lies inside it. This warm emission from the cavity could be driven by shocks or by photon heating of the cavity walls. The flanks of the H_2 redshifted bow shock connect with the cavity edges, giving support to the scenario where the cavity is created

by the entrainment of jet-driven bow shocks. This is at variance with the blueshifted lobe, where the expansion of both the collimated jet and the wide-angle molecular shells driven by the two sources concur to create the asymmetric CO cavity observed with ALMA.

7. The spectrum of the nonresolved binary system shows deep structured ice bands and CO $v = 1-0$ and H_2O $v = 1-0$ gaseous lines in absorption, likely originating in the envelope or disk intercepting the warm mid-IR continuum. Several hydrogen recombination lines of the Paschen and Brackett series are observed on source. Their emission peaks shift from being outflow dominated to being accretion dominated as the energy of the line increases.

This paper shows the richness of information that can be gathered with JWST observations on a complex system such as HH46. We have in particular unveiled the central engine of the HH46 IRS outflow, showing that jet entrainment and wide-angle winds from the two sources are both at play in shaping the large-scale structure of the outflow. The obtained data demonstrate the power of JWST in the investigation of embedded regions around young Class I protostars, which remain elusive even at near-IR wavelengths. A series of forthcoming papers currently in preparation will examine in depth a number of topics highlighted in this article, including the excitation and dynamics of the H_2 outflow and of the atomic jet, as well as the nature of the gas and dust features of the source.

Acknowledgments

This work is based on observations made with the NASA/ESA/CSA James Webb Space Telescope. The data were obtained from the Mikulski Archive for Space Telescopes at the Space Telescope Science Institute, which is operated by the Association of Universities for Research in Astronomy, Inc., under NASA contract NAS 5–03127 for JWST. These observations are associated with program #1706 and can be accessed via DOI:10.17909/eav1-0619.

P.H., T.G., and H.A. acknowledge funding support from JWST GO program #1706 provided by NASA through a grant from the Space Telescope Science Institute. We gratefully acknowledge the help of the Space Telescope Science Institute JWST Helpdesk, and in particular Jane Morrison, for her valuable suggestions on the NIRSpec data reduction. INAF coauthors acknowledge support from the Large Grant INAF 2022 "YSOs Outflows, Disks, and Accretion: toward a global framework for the evolution of planet-forming systems (YODA)" and from PRIN MUR 2022 20228JPA3A "The path to star and planet formation in the JWST era (PATH)." L.P. acknowledges the PRIN MUR 2022 FOSSILS (Chemical origins: linking the fossil composition of the Solar System with the chemistry of protoplanetary disks, Prot. 2022JC2Y93). E.v.D. acknowledges the funding from the European Research Council (ERC) under the European Union's Horizon 2020 research and innovation program (grant agreement No. 291141 MOLDISK). S.C. gratefully acknowledges support from the Programme National de Physique et Chimie du Milieu Interstellaire (PCMI), cofunded by CNRS-INSU, CNES, and CEA, and from Observatoire de Paris (Action Fédératrice Incitative Univers Froid). T.P.R. acknowledges support from the ERC (grant agreement No. 743029 EASY). C.F.M. is funded by the European Union (ERC, WANDA, 101039452). Views and opinions expressed are however those of the author(s) only and do not necessarily reflect those of the European Union or the European Research Council Executive Agency. Neither the European Union nor the granting authority can be held responsible for them. This paper makes use of the following ALMA data: ADS/JAO.ALMA #2012.1.00382.S. ALMA is a partnership of ESO (representing its member states), NSF (USA), and NINS (Japan), together with NRC (Canada), NSC and ASIAA (Taiwan), and KASI (Republic of Korea), in cooperation with the Republic of Chile. The Joint ALMA Observatory is operated by ESO, AUI/NRAO, and NAOJ. This work benefited from the Core2disk-III residential program of Institut Pascal at Universiteé Paris-Saclay, with the support of the program "Investissements d'avenir" ANR-11-IDEX-0003-01.

Facilities: JWST, HST, ALMA.

Appendix A
The HH46 IRS Extracted Spectrum and Comparison with Spitzer

Figure 14 shows the MIRI (upper panel) and NIRSpec (lower panel) spectrum extracted at the HH46 IRS position, using an aperture proportional to $1.22\lambda/D$. The figure plots the spectra of the individual subchannels (MIRI) and gratings (NIRSpec) as well as the final spectrum obtained by rescaling them to the MIRI Channel 1 SHORT spectrum. The figure also reports the Spitzer spectrum of the source for comparison, as well as mid-IR photometry from different facilities. The difference between the Spitzer and JWST spectra might be due to the source variability or to different extraction procedures.

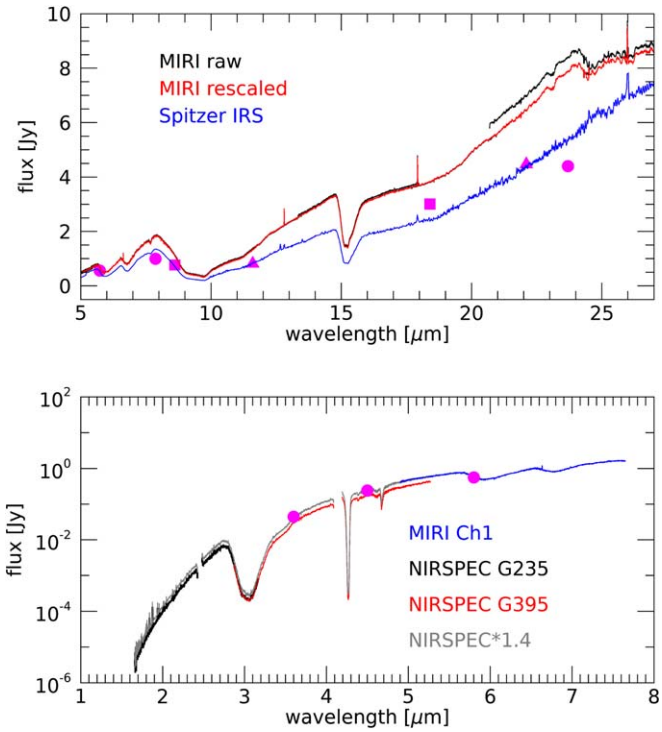

Figure 14. The upper panel shows the MIRI spectra in the individual subchannels (black lines) and the final complete spectrum obtained by rescaling the individual subspectra to the Channel 1 SHORT (red line). The figure also displays the Spitzer IRS spectrum from Noriega-Crespo et al. (2004; in blue) as well as archival photometric points from Spitzer IRAC and MIPS (circles), WISE (triangles) and AKARI (squares). The bottom panel displays the NIRSpec G235 (black) and G395 (red) spectra in comparison with the MIRI Channel 1 spectrum (blue). The NIRSpec spectrum rescaled to match MIRI and the IRAC photometric points are indicated in gray.

Appendix B
Spectra of the Jet and H_2 Peak

Figures 15 and 16 show the NIRSpec and MIRI spectra extracted from a circular aperture of 0.″4 in radius at the position of the B2 jet knot ($08^h25^m43^s.88$, $-51°00'34.''55$) and the H_2 A1 peak ($08^h25^m43^s.86$, $-51°00'35.''69$), respectively. These circular apertures are drawn in Figures 2 and 7.

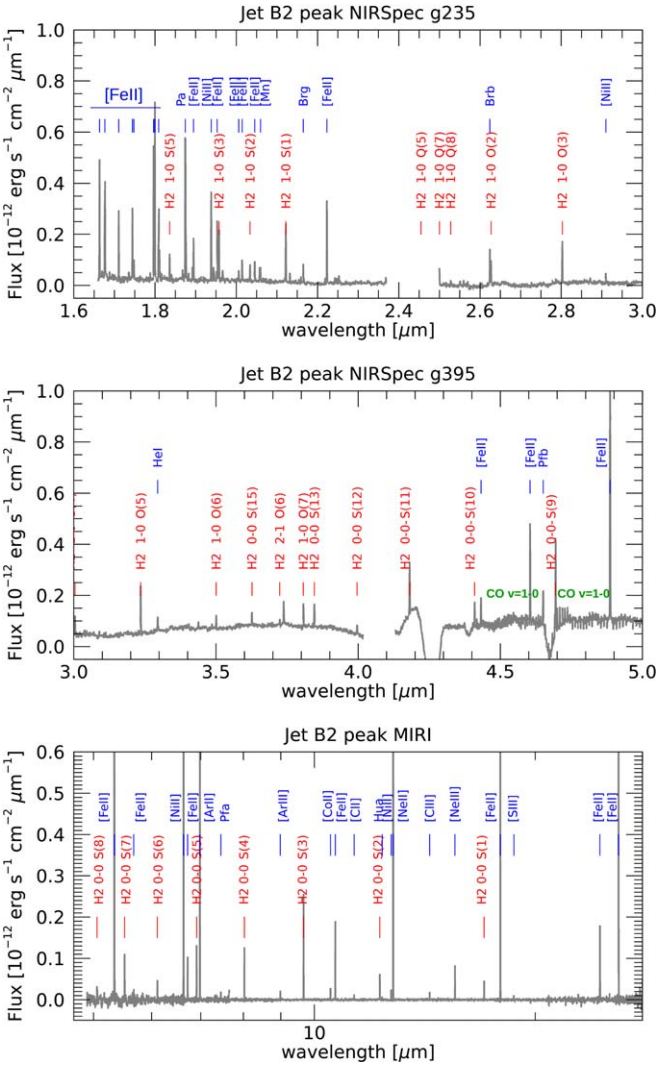

Figure 15. Complete NIRSpec and MIRI spectrum extracted from a circular aperture of 0.″4 in radius centered on the B2 knot of the blueshifted jet, with the major detected atomic (blue) and molecular (red for H_2 and green for CO) lines indicated. The MIRI spectrum has been continuum subtracted.

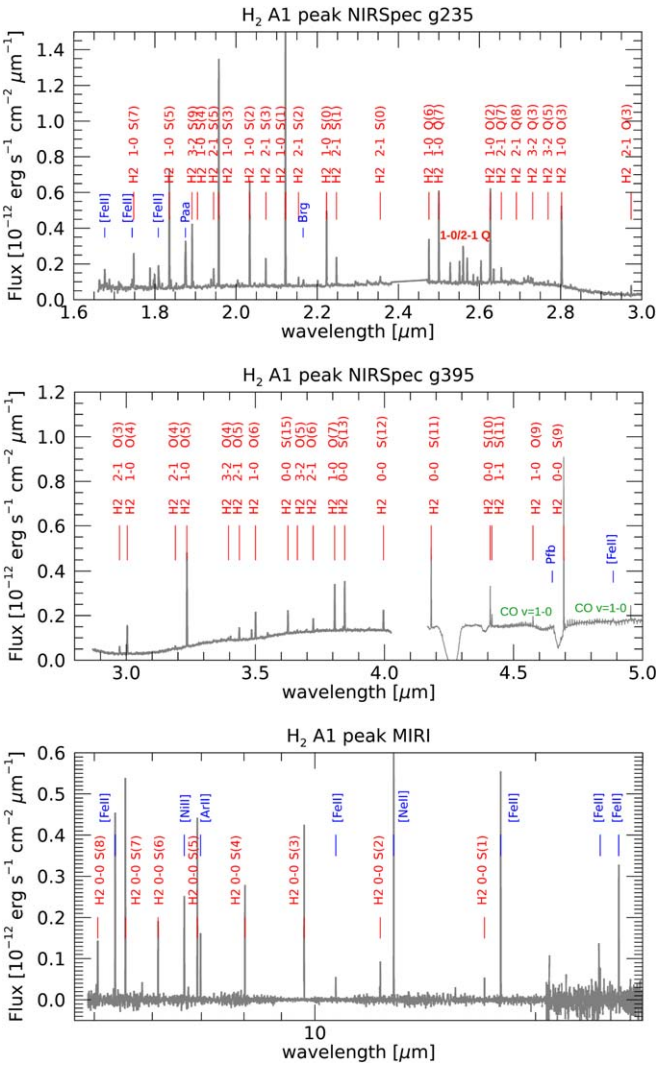

Figure 16. The same as Figure 15 but for an aperture centered at the peak of the H_2 knot A1.

Appendix C
Line List

In Table 1 we list all the atomic lines detected in the blueshifted jet, with their identification and relative intensity with respect to the [Fe II] 5.3 μm line. Table 2 summarizes the H_2 transitions detected in the A1 knot, listed by vibrational level.

Table 1
List of Detected Atomic Lines in the Jet

Ion	I.P.[b] (eV)	Line ID	λ(vac) (μm)	T_{ex}[a] (K)	$I_\lambda/I_{[\mathrm{Fe\ II}]5.3\ \mu m}$	Grism/Chan
[Fe II]	7.90	$a^4D_{1/2}$-$a^4F_{5/2}$	1.66422497	4083.22	0.05163	G235
		$a^4D_{5/2}$-$a^4F_{7/2}$	1.8098952	11445.92	0.06823	G235
		$a^4D_{5/2}$-$a^4F_{3/2}$	1.8959259	12074.14	0.025969	G235
		$a^4D_{7/2}$-$a^4F_{5/2}$	1.9541410	11445.92	0.03822	G235
		$a^2P_{1/2}$-$a^4P_{1/2}$	2.0072612	27173.82	0.007018	G235
		$a^2H_{9/2}$-$a^2G_{9/2}$	2.0156760	29934.82	0.013035	G235
		$a^2P_{3/2}$-$a^4P_{5/2}$	2.0465833	26416.83	0.01385	G235
		$a^4F_{3/2}$-$a^6D_{3/2}$	4.4348339	4485.36	0.00996	G395
		$a^4F_{7/2}$-$a^6D_{7/2}$	4.8891395	3496.42	0.065055	G395
		$a^4F_{5/2}$-$a^6D_{3/2}$	5.0623456	4083.22	0.01959	ch1-SHORT
		$a^4F_{9/2}$-$a^6D_{9/2}$	5.3401693	2694.25	1.	ch1-SHORT
		$a^4F_{7/2}$-$a^6D_{5/2}$	5.6739070	3496.42	0.01162	ch1-SHORT
		$a^4F_{9/2}$-$a^6D_{7/2}$	6.721277	2694.25	0.04997	ch1-LONG
		$a^6D_{5/2}$-$a^6D_{9/2}$	14.977170	960.65	0.001018	ch3-MEDIUM
		$a^4F_{7/2}$-$a^4F_{9/2}$	17.92324	3496.42	0.93672	ch3-LONG
		$a^4F_{5/2}$-$a^4F_{7/2}$	24.5019	4083.22	0.254099	ch4-LONG
		$a^6D_{7/2}$-$a^6D_{9/2}$	25.988390	553.62[c]	0.90017	ch4-LONG
[Ni II]	7.64	$^2F_{7/2}$-$^4F_{9/2}$	1.93930	19495.97	0.05259	G235
		$^2F_{7/2}$-$^4F_{5/2}$	2.91144	19495.97	0.005496	G235
		$^2D_{3/2}$-$^2D_{5/2}$	6.6360	2168.15	0.36327	ch1-LONG
		$^4F_{7/2}$-$^4F_{9/2}$	10.6822	13423.83	0.066096	ch2-LONG
		$^4F_{5/2}$-$^4F_{7/2}$	12.7288	14554.16	0.01096	ch3-SHORT
[Mn II]	7.43	a^5D_4-a^5S_2	2.06063	20611.69	0.015145	G235
[Ar II]	15.76	$^2P_{1/2}$-$^2P_{3/2}$	6.985274	2059.73[c]	0.3737	ch1-LONG
[Ar III]	27.63	$^3P_1$-$^3P_2$	8.99138	1600.17[c]	0.006188	ch2-MEDIUM
[Co II]	7.88	a^3F_3-a^3F_4	10.522727	1367.30[c]	0.0093048	ch2-LONG
		a^5F_4-a^5F_5	14.7287	5796.81	0.002452	ch3-MEDIUM
		a^3F_2-a^3F_3	15.45898	2298.01	0.002789	ch3-MEDIUM
[Cl I]	0	$^2P_{1/2}$-$^2P_{3/2}$	11.333352	1269.51[c]	0.0044875	ch2-LONG
[Cl II]	23.81	$^3P_1$-$^3P_2$	14.3678	1001.39[c]	0.011506	ch3-MEDIUM
[Ne II]	21.56	$^2P_{1/2}$-$^2P_{3/2}$	12.813548	1122.85[c]	0.89572	ch3-SHORT
[Ne III]	40.96	$^3P_1$-$^3P_2$	15.55505	924.96[c]	0.044233	ch3-LONG
[S I]	0	$^3P_1$-$^3P_2$	25.2490	569.83[c]	0.01844	ch4-LONG
[S III]	23.24	$^3P_2$-$^3P_1$	18.71303	1198.59	0.008877	ch4-SHORT
HI	13.598	Paα (4-3)	1.875613	97492.31	0.097326	G235
		Brγ (7-4)	2.166120	107440.45	0.007486	G235
		Brβ (6-4)	2.625867	106632.17	0.018529	G235
		Pfβ (7-5)	4.653778	107440.45	0.008137	G395
		Pfα (6-5)	7.459858	153419.72	0.011506	ch1-LONG
		Huα (7-6)	12.371898	154582.66	0.004055	ch3-SHORT

Notes.
[a] Excitation temperature of the upper level.
[b] Ionization potential of the X^{i-1} ion.
[c] Fundamental transition to the ground state.

Table 2
Summary of the H_2 Lines Detected in the Molecular Peak

v_u-v_l	Rot. Lines	T_{ex}[K] min-max[a]
0–0	S(1)-S(15)	354–1.5e4
1–0	S(0)-S(9), Q(1)-Q(13),O(2)-O(9)	4160–1.1e4
2–1	S(0)-S(8),Q(1)-Q(8),O(3)-O(6)	8087–1.4e4
3–2	S(1)/S(3)/S(9),Q(3)/Q(5),O(4)/O(5)	1.2e4–1.3e4

Note.
[a] Minimum and maximum excitation temperature of the upper level.

ORCID iDs

Brunella Nisini https://orcid.org/0000-0002-9190-0113
Maria Gabriela Navarro https://orcid.org/0000-0002-1860-2304
Teresa Giannini https://orcid.org/0000-0002-7035-8513
Simone Antoniucci https://orcid.org/0000-0002-0666-3847
Patrick, J. Kavanagh https://orcid.org/0000-0001-6872-2358
Patrick Hartigan https://orcid.org/0000-0002-5380-549X
Francesca Bacciotti https://orcid.org/0000-0001-5776-9476
Alessio Caratti o Garatti https://orcid.org/0000-0001-8876-6614
Alberto Noriega-Crespo https://orcid.org/0000-0002-6296-8960
Ewine F. van Dishoeck https://orcid.org/0000-0001-7591-1907
Emma T. Whelan https://orcid.org/0000-0002-3741-9353
Hector G. Arce https://orcid.org/0000-0001-5653-7817
Sylvie Cabrit https://orcid.org/0000-0002-1593-3693
Deirdre Coffey https://orcid.org/0000-0002-2210-202X
Davide Fedele https://orcid.org/0000-0001-6156-0034
Jochen Eislöffel https://orcid.org/0000-0001-6496-0252
Maria Elisabetta Palumbo https://orcid.org/0000-0002-9122-491X
Linda Podio https://orcid.org/0000-0003-2733-5372
Tom P. Ray https://orcid.org/0000-0002-2110-1068
Riccardo G. Urso https://orcid.org/0000-0001-6926-1434
Juan M. Alcalá https://orcid.org/0000-0001-8657-095X
Manuel A. Bautista https://orcid.org/0000-0001-6837-3055
Claudio Codella https://orcid.org/0000-0003-1514-3074
Thomas P. Greene https://orcid.org/0000-0002-8963-8056
Carlo F. Manara https://orcid.org/0000-0003-3562-262X

References

Agra-Amboage, V., Cabrit, S., Dougados, C., et al. 2014, A&A, 564, A11
Alcalá, J. M., Manara, C. F., Natta, A., et al. 2017, A&A, 600, A20
Antoniucci, S., Nisini, B., Giannini, T., & Lorenzetti, D. 2008, A&A, 479, 503
Antoniucci, S., Nisini, B., Giannini, T., et al. 2017, A&A, 599, A105
Arce, H. G., Mardones, D., Corder, S. A., et al. 2013, ApJ, 774, 39
Argyriou, I., Glasse, A., Law, D. R., et al. 2023, A&A, 675, A111
Bai, X.-N., Ye, J., Goodman, J., & Yuan, F. 2016, ApJ, 818, 152
Bally, J. 2016, ARA&A, 54, 491
Banzatti, A., Abernathy, K. M., Brittain, S., et al. 2022, AJ, 163, 174
Birney, M., Whelan, E., Dougados, C., Nisini, B., & Cabrit, S. 2024, A&A, submitted
Böker, T., Arribas, S., Lützgendorf, N., et al. 2022, A&A, 661, A82
Boogert, A. C. A., Pontoppidan, K. M., Lahuis, F., et al. 2004, ApJS, 154, 359
Bushouse, H., Eisenhamer, J., Dencheva, N., et al. 2023, JWST Calibration Pipeline, v1.9.6, Zenodo, doi:10.5281/zenodo.7714020
de Valon, A., Dougados, C., Cabrit, S., et al. 2022, A&A, 668, A78
Dionatos, O., Nisini, B., Cabrit, S., Kristensen, L., & Pineau Des Forêts, G. 2010, A&A, 521, A7
Eislöffel, J., Davis, C. J., Ray, T. P., & Mundt, R. 1994, ApJL, 422, L91
Eislöffel, J., & Mundt, R. 1994, A&A, 284, 530
Erkal, J., Nisini, B., Coffey, D., et al. 2021, ApJ, 919, 23
Federman, S., Megeath, S. T., Rubinstein, A. E., et al. 2024, ApJ, 966, 41
Ferreira, J. 1997, A&A, 319, 340
Francis, L., van Gelder, M. L., van Dishoeck, E. F., et al. 2024, A&A, 683, A249
Frank, A., Ray, T. P., Cabrit, S., et al. 2014, in Protostars and Planets VI, ed. H. Beuther et al. (Tucson, AZ: Univ. of Arizona Press), 451
Garcia Lopez, R., Nisini, B., Eislöffel, J., et al. 2010, A&A, 511, A5
Gasman, D., Argyriou, I., Sloan, G. C., et al. 2023, A&A, 673, A102
Giannini, T., Nisini, B., Neufeld, D., et al. 2011, ApJ, 738, 80
Glassgold, A. E., Najita, J. R., & Igea, J. 2007, ApJ, 656, 515
Grant, S. L., van Dishoeck, E. F., Tabone, B., et al. 2023, ApJL, 947, L6
Greene, T. P., Gully-Santiago, M. A., & Barsony, M. 2018, ApJ, 862, 85
Hartigan, P., Frank, A., Foster, J. M., et al. 2011, ApJ, 736, 29
Hartigan, P., Heathcote, S., Morse, J. A., Reipurth, B., & Bally, J. 2005, AJ, 130, 2197
Hartigan, P., Raymond, J., & Hartmann, L. 1987, ApJ, 316, 323
Heathcote, S., Morse, J. A., Hartigan, P., et al. 1996, AJ, 112, 1141
Helmich, F. P., van Dishoeck, E. F., Black, J. H., et al. 1996, A&A, 315, L173
Hollenbach, D., & Gorti, U. 2009, ApJ, 703, 1203
Hollenbach, D., & McKee, C. F. 1989, ApJ, 342, 306
Jakobsen, P., Ferruit, P., Alves de Oliveira, C., et al. 2022, A&A, 661, A80
Lee, C.-F. 2020, A&ARv, 28, 1
Liu, C.-F., Shang, H., Herczeg, G. J., & Walter, F. M. 2016, ApJ, 832, 153
Masciadri, E., & Raga, A. C. 2002, ApJ, 568, 733
Maurri, L., Bacciotti, F., Podio, L., et al. 2014, A&A, 565, A110
McClure, M. K., Rocha, W. R. M., Pontoppidan, K. M., et al. 2023, NatAs, 7, 431
Nisini, B. 2003, Ap&SS, 287, 207
Nisini, B., Antoniucci, S., Giannini, T., & Lorenzetti, D. 2005, A&A, 429, 543
Nisini, B., Giannini, T., Antoniucci, S., et al. 2016, A&A, 595, A76
Nisini, B., Santangelo, G., Giannini, T., et al. 2015, ApJ, 801, 121
Noriega-Crespo, A., Morris, P., Marleau, F. R., et al. 2004, ApJS, 154, 352
Pascucci, I., Cabrit, S., Edwards, S., et al. 2023, in ASP Conf. Ser. 534, Protostars and Planets VII, ed. S. Inutsuka et al. (San Francisco, CA: ASP), 567
Patapis, P., Argyriou, I., Law, D. R., et al. 2024, A&A, 682, A53
Pelletier, G., & Pudritz, R. E. 1992, ApJ, 394, 117
Perna, M., Arribas, S., Marshall, M., et al. 2023, A&A, 679, 89
Podio, L., Tabone, B., Codella, C., et al. 2021, A&A, 648, A45
Rabenanahary, M., Cabrit, S., Meliani, Z., & Pineau des Forêts, G. 2022, A&A, 664, A118
Ray, T. P., McCaughrean, M. J., Caratti o Garatti, A., et al. 2023, Natur, 622, 48
Reipurth, B., Yu, K. C., Heathcote, S., Bally, J., & Rodríguez, L. F. 2000, AJ, 120, 1449
Rieke, G. H., Wright, G. S., Böker, T., et al. 2015, PASP, 127, 584
Rigliaco, E., Pascucci, I., Duchene, G., et al. 2015, ApJ, 801, 31
Rocha, W. R. M., van Dishoeck, E. F., Ressler, M. E., et al. 2024, A&A, 683, 124
Salyk, C., Herczeg, G. J., Brown, J. M., et al. 2013, ApJ, 769, 21
Shang, H., Krasnopolsky, R., Liu, C.-F., & Wang, L.-Y. 2020, ApJ, 905, 116
Shang, H., Liu, C.-F., Krasnopolsky, R., & Wang, L.-Y. 2023, ApJ, 944, 230
Tabone, B., Bettoni, G., van Dishoeck, E. F., et al. 2023, NatAs, 7, 805
Tychoniec, L., van Gelder, M. L., van Dishoeck, E. F., et al. 2024, arXiv:2402.04343
Urso, R. G., Hénault, E., Brunetto, R., et al. 2022, A&A, 668, A169
van Dokkum, P. G. 2001, PASP, 113, 1420
van Kempen, T. A., Kristensen, L. E., Herczeg, G. J., et al. 2010, A&A, 518, L121
van Kempen, T. A., van Dishoeck, E. F., Güsten, R., et al. 2009, A&A, 501, 633
Velusamy, T., Langer, W. D., & Marsh, K. A. 2007, ApJL, 668, L159
Watson, D. M., Calvet, N. P., Fischer, W. J., et al. 2016, ApJ, 828, 52
Wright, G. S., Rieke, G. H., Glasse, A., et al. 2023, PASP, 135, 048003
Yang, Y.-L., Green, J. D., Pontoppidan, K. M., et al. 2022, ApJL, 941, L13
Zhang, Y., Arce, H. G., Mardones, D., et al. 2016, ApJ, 832, 158
Zhang, Y., Arce, H. G., Mardones, D., et al. 2019, ApJ, 883, 1